Numerical Simulations of a Landfalling Cold Front Observed during COAST: Rapid Evolution and Responsible Mechanisms*

BRIAN A. COLLE

Institute for Terrestrial and Planetary Atmospheres, State University of New York at Stony Brook, Stony Brook, New York

BRADLEY F. SMULL

NOAA/National Severe Storms Laboratory, and Department of Atmospheric Sciences, University of Washington, Seattle, Washington

MING-JEN YANG

Department of Atmospheric Sciences, Chinese Culture University, Taipei, Taiwan

(Manuscript received 9 May 2001, in final form 11 January 2002)

ABSTRACT

This paper identifies mechanisms that led to the observed rapid evolution of a landfalling weak cold front along the steep mountainous northern California coast on 1 December 1995. This event was simulated down to 3-km horizontal grid spacing using the Pennsylvania State University–NCAR Mesoscale Model version 5 (MM5). The MM5 simulation reproduced the basic features such as the timing, location, and orientation of the cold front and associated precipitation evolution, as well as the tendency for enhanced precipitation to extend ~50–100 km upwind of the coastal barrier, with the heaviest amounts occurring over the windward slopes (0–20 km inland); locally, however, the model underestimated the magnitude of the prefrontal terrain-enhanced flow by as much as 30% since the simulated low-level static stability was weaker than observed.

The MM5 simulations illustrate the complex thermal, wind, and precipitation structures in the coastal zone. Upstream flow blocking by the steep coastal terrain led to the development of a mesoscale pressure ridge and prefrontal terrain-enhanced winds exceeding 25 m s^{-1}. Because of the irregular coastline and highly three-dimensional terrain, the low-level winds were not uniform along the coast. Rather, prefrontal southerly flow was significantly reduced downwind of the major capes (viz. Mendocino and Blanco), while there were localized downgradient accelerations adjacent to regions of higher topography along uninterrupted stretches of coastline. Terrain–front interactions resulted in a slowing of the front as the system made landfall, and blocking contributed to a ''tipped forward'' baroclinic structure below 800 mb.

The MM5 was used to investigate some of the reasons for the rapid intensification of the frontal temperature gradient and banded precipitation in the coastal zone. During this event the large-scale vertical motions increased in an environment favorable for moist convection, and a simulation without coastal topography illustrated rapid development of coastal precipitation even in the absence of local terrain influences. The coastal topography helped to further enhance and collapse the thermal gradient and associated cold-frontal rainband through enhanced deformation frontogenesis associated with the prefrontal terrain-enhanced flow. Diabatic effects from precipitation are also shown to have been important in organizing the precipitation in the coastal zone and further enhancing the frontal temperature gradient.

1. Introduction

One of the major objectives of the Coastal Observation and Simulation with Topography (COAST) field program was to study how landfalling fronts and cyclones are modified by the orography of the U.S. west coast (Bond et al. 1997). This paper is a continuation of the Yu and Smull (2000) study (herein after denoted YS), which used conventional synoptic observations as well as profiler, ground-based, and National Oceanic and Atmospheric Administration (NOAA) P-3 airborne Doppler radars to describe the mesoscale structure and evolution of a landfalling frontal system along the northern California coast on 1 December 1995. The study area for this event focused on a section of coastline characterized by a steep rise of terrain to >1600 m MSL within 120 km of the shore (see YS's Fig. 1), which favors the development of terrain-enhanced winds and heavy rainfall over the coastal zone. As the front made landfall it exhibited a southwest to northeast orientation, and the low-level prefrontal flow approaching the coast

* Marine Sciences Research Center Contribution Number 1242.

Corresponding author address: Dr. B. A. Colle, Institute for Terrestrial and Planetary Atmospheres, Marine Sciences Research Center, SUNY—Stony Brook, Stony Brook, NY 11794-5000.
E-mail: bcolle@notes.cc.sunysb.edu

was partially deflected and accelerated adjacent to the steep topography.

Some of the principal findings of YS include the following.

1) The partially blocked low-level flow by the steep coastal terrain resulted in a confluent wind transition ~20 km offshore from southwesterly to south-southwesterly eastward across this transition. The maximum wind speeds enhanced by terrain reached 26–28 m s^{-1} at 0.75 km MSL immediately east of the confluent wind transition.
2) Flow blocking by the coastal terrain appeared to enhance the precipitation in the vicinity of the front, including the rapid genesis of a narrow cold-frontal rainband (NCFR). This trend was closely related to the low-level convergence of the cross-shore flow component, which was enhanced as the terrain blocking increased adjacent to the steeper coastal topography. Furthermore, prefrontal terrain-enhanced flow also led to a cross-frontal shear profile that favored more upright convection along the NCFR with the advancing cool air mass [reminiscent of processes occurring along gust fronts in warm season convective systems as described by Rotunno et al. (1988)].
3) Cumulative radar statistics showed evidence of a systematic increase in precipitation toward the shore, with mean radar reflectivities within ~40 km of the coast 20%–30% larger than those farther offshore.

Frontal modification near steep topography can result from a wide variety of mechanisms. The most examined terrain effect on fronts, which YS also addressed, is the role of upstream flow blocking on low-level frontal movement, deformation, and intensity. In terms of relevant scaling parameters, hydrodynamically steep topography exists when the Burger number [$B = N_m h/fL$, where h is the terrain height, N_m is the moist static stability (Durran and Klemp 1982), and L is the mountain half-width] exceeds unity. In the rotating case blocked flow is characterized by a $N_m h/U \gg 1$ (inverse Froude number) regime (Pierrehumbert and Wyman 1985; Overland and Bond 1995), which extends upstream of the barrier crest approximately a Rossby radius, $L_r = N_m h/f$. Both recent theoretical (Braun et al. 1999a) and modeling studies (Colle et al. 1999) have suggested that low-level blocking and deflection by steep coastal topography can lead to upstream frontogenesis, mainly through enhanced deformation. For example, using a 3-km Pennsylvania State University–National Center for Atmospheric Research (Penn State–NCAR) fifth-generation Mesoscale Model (MM5) simulation of COAST Intensive Observing Period 5 (IOP5), Colle et al. (1999) showed that southerly prefrontal flow deflection around the nearly circular Olympic Mountains of western Washington led to enhanced deformation and frontogenesis along the lower windward slopes. Braun et al. (1999a) used two-dimensional idealized simulations to show that the steep California coastal range favors strong deceleration of the fronts and weak windward frontogenesis. Braun et al. further showed that the broad horizontal scale of the western U.S. terrain helps enhance the flow blocking and barrier jet in the coastal zone.

Doyle (1997) showed that reduced surface roughness over water compared to flat land resulted in a 30% increase in the terrain-enhanced flow over the coastal waters. Spatial variations in surface frictional effects, such as a surface-roughness discontinuity at a coastline, have been shown to contribute to frontogenesis, especially if the progression of the front is slow and the front is orientated nearly parallel to the coast (Roeloffzen et al. 1986; Okland 1990). Braun et al. (1999b) showed that the coastal roughness change resulted in an enhancement of the frontal updraft and stronger frontal retardation; however, most frontal changes were primarily associated with orographic effects.

Diabatic processes associated with precipitation can also modify low-level frontal evolution. Recent studies have also shown that differential latent heating across the front including latent cooling processes (sublimation and melting of ice and evaporation of rain) immediately behind the front can enhance or maintain frontal intensity (Barth and Parsons 1996; Buzzi et al. 1998; Colle et al. 1999). For example, Colle et al. (1999) showed that latent cooling from falling hydrometeors was important in maintaining the frontal intensity and NCFR as the front pushed southward along the east side of the Olympic Mountains. Other studies have shown that latent heating can enhance ageostrophic frontal circulations and result in more rapid frontogenesis (Knight and Hobbs 1988; Parker and Thorpe 1995a).

Finally, changes in the synoptic-scale forcing can play an important role in frontal evolution even in the absence of terrain. Ironically, there have been few studies that have attempted to quantify the large-scale versus mesoscale topographic influences as a front approaches steep terrain. Schumacher et al. (1996) found in a statistical analysis of frontal passages over the Appalachians that the strength of the upper-level potential vorticity anomaly primarily determined the movement of the front across this relatively modest barrier, not low-level terrain blocking as determined by the Froude number.

It is difficult to separate these factors that influence frontal evolution using only high-resolution observations provided by the COAST experiment. For example, although the detailed kinematic observations around the front in YS suggested that the front intensified as it approached the steep coastal terrain, not enough in situ thermal observations were available to make a detailed assessment of the responsible mechanisms for the rapid frontal evolution. Furthermore, there have been relatively few three-dimensional modeling studies looking at the interaction of fronts with orography. Using high-resolution simulations of a 7 January 1995 landfalling frontal case along the California coast, Doyle (1997) showed that terrain-enhanced flow retarded the south-

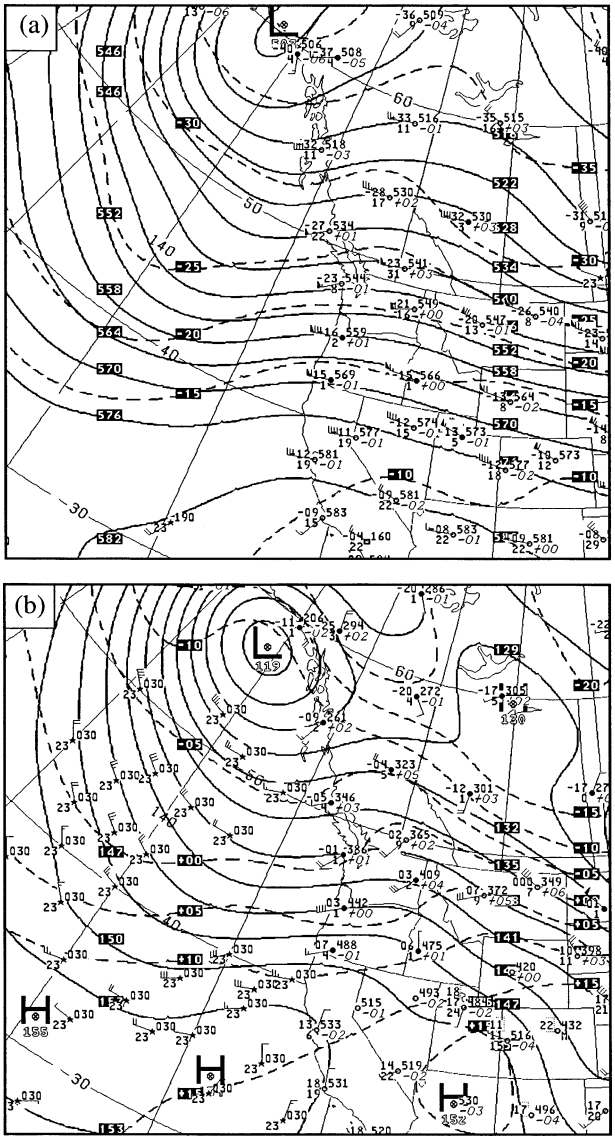

FIG. 1. (a) NCEP analysis at 500 mb showing geopotential height (solid every 6 dam) and temperature (dashed every 5°C) for 0000 UTC 1 Dec 1995. (b) Same as in (a) except for 850 mb and geopotential height is contoured every 3 dam. (c) Manual surface analysis for 0000 UTC 1 Dec 1995. Sea level pressure and temperature are contoured every 4 mb and 2°C, respectively, and the plotted data at each station include temperature (°C), dewpoint (°C), wind (1 full barb = 10 kt and 1 kt = 0.515 m s^{-1}), sea level pressure, 3-h pressure change, cloud cover, and present weather.

ward frontal propagation near the coast relative to farther offshore. Unfortunately, no high-resolution observations were available for detailed verification of the simulated flow above the surface and offshore frontal structures in Doyle's case. His event also focused over the central California coastal terrain, which is not as steep and wide as the coastal terrain near the Oregon–California border as examined in YS.

High-resolution numerical simulations of the 1 December 1995 COAST case offer the opportunity for detailed comparison with surface, in situ, and Doppler radar observations along the northern California coast to verify the model; subsequently, these model runs can be used to investigate the transient structure of the terrain-enhanced flow and the frontal precipitation bands observed by YS. As such, this study serves to extend their work by addressing the following questions:

- What were the comparative roles of local topographic (blocking) effects versus synoptic-scale contributions to the frontal and precipitation evolution in the coastal zone?
- How did the terrain enhanced flow along the coast evolve as the front approached?
- Were there any diabatic contributions to the evolution of the frontal thermal and precipitation structures?

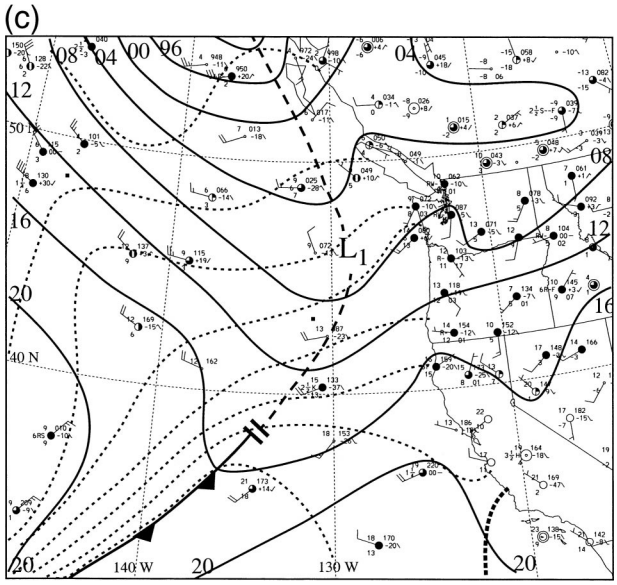

FIG. 1. (*Continued*)

Yu and Smull (2000) provide detailed observations of the mesoscale structures of the frontal system observed on 1 December 1995; therefore, only limited observations will be presented to provide additional context for the MM5 simulations discussed herein.

2. Synoptic-scale overview

At 0000 UTC 1 December 1995, which is about 6 h before the NOAA P-3 aircraft began collecting data along the southern Oregon coast, a short-wave 500-mb trough extended southwest of the British Columbia coast and a weak ridge was situated over the western United States (Fig. 1a). At 850 mb (Fig 1b), a baroclinic trough was located upstream of the U.S. west coast around 135°W, which is 150–300 km east of the trough at 500 mb. The 850-mb temperature gradient extended eastward toward the coast and appeared relatively broad and uniform in the north–south direction. A surface trough

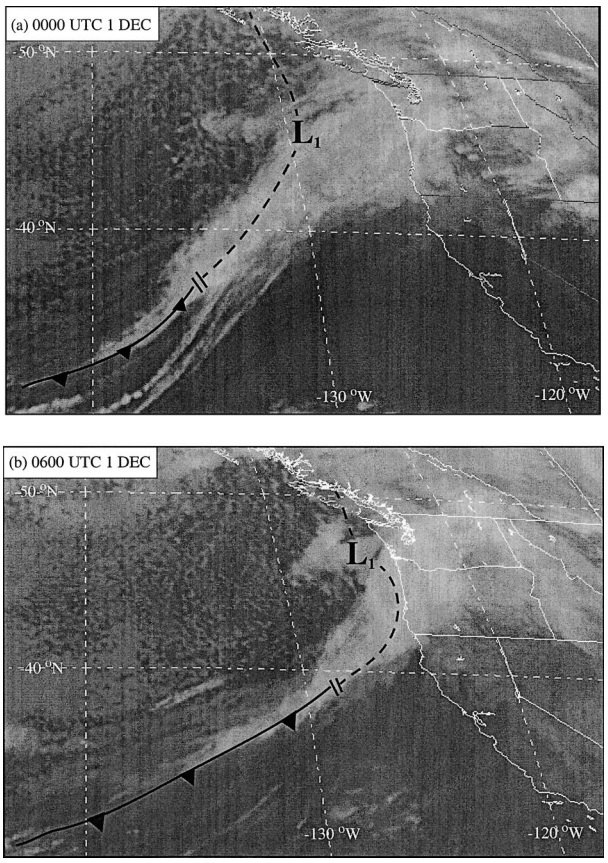

FIG. 2. Infrared satellite images for (a) 0000 and (b) 0600 UTC 1 Dec 1995. The position of the surface disturbance L_1 and surface front/trough are estimated using surface observations and the inflection in mid- and upper-level clouds.

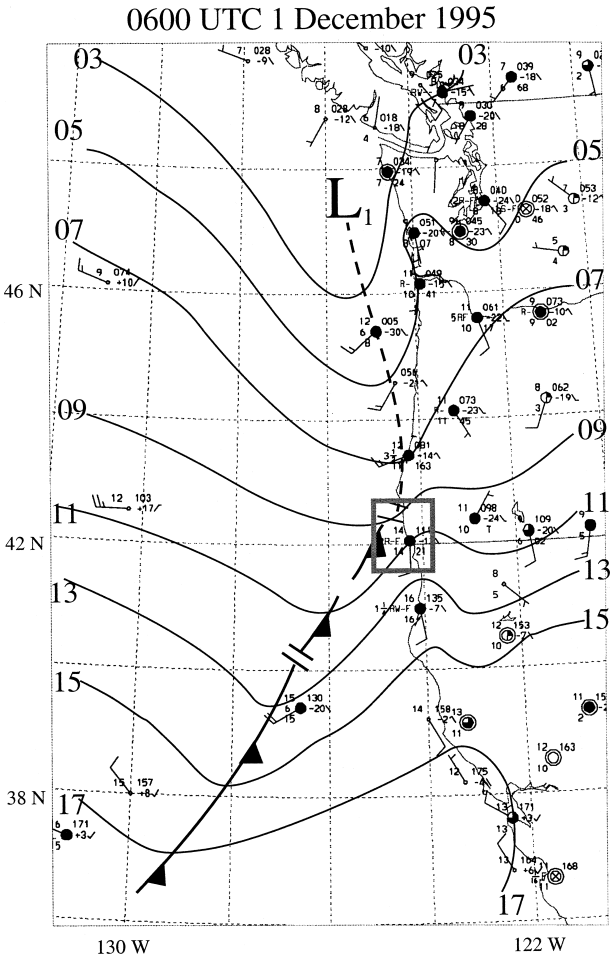

FIG. 3. Manual surface analysis for 0600 UTC 1 Dec 1995 showing sea level pressure contoured every 2 mb. The gray box indicates the P-3 Doppler region for Fig. 5.

extended along 130°W between 40° and 50°N (Fig. 1c). An infrared satellite image at 0000 UTC 1 December 1995 (Fig. 2) suggests that the low-level comma head of cloudiness to the west of the upper-level baroclinic cloud shield was associated with a northern surface wave (L_1) located approximately 500 km west of the Washington coast. An isotherm analysis derived from surface time series (not shown) suggests that the surface trough to the south 40°N had weak cold frontal characteristics (Fig. 1c).[1]

By 0600 UTC 1 December (Fig. 3), the surface trough axis had reached the southern Oregon coast. As will be discussed in more detail in conjunction with evaluation of simulation results in section 4, the wind and temperature transitions along the southern Oregon coast around this time indicate a gradual veering from southwesterly to westerly and a slight temperature drop during trough passage. Meanwhile, as detailed in the following section and by YS, the cold front was intensifying rapidly between the south Oregon coast and 40°N. Overall, the upper-level cloud shield decreased in spatial extent during the previous 6 h (Fig. 2b), which suggests that the baroclinic wave was evolving rapidly as it approached the coast.

By 1200 UTC 1 December (Fig. 4a), the analyzed geopotential trough at 850 mb had flattened offshore of the California coast near 130°W, resulting in nearly zonal flow over the far eastern Pacific. Meanwhile, the west–east temperature gradient had increased along the west coast with the amplification of the thermal ridge over the western United States, and weak cold advection was located as far south as Oakland, California (OAK).

3. Mesoscale overview

Using airborne Doppler radar data, YS showed the rapid intensification of the wind shift near the northern California coast and the associated development of an NCFR. It is important that the model properly simulate this evolution; therefore, two key dual-Doppler P-3 radar analyses at 0.75 km MSL are shown for model val-

[1] Frontal positions referenced in this study were determined by the leading edge of cyclonic shear and weak cold advection.

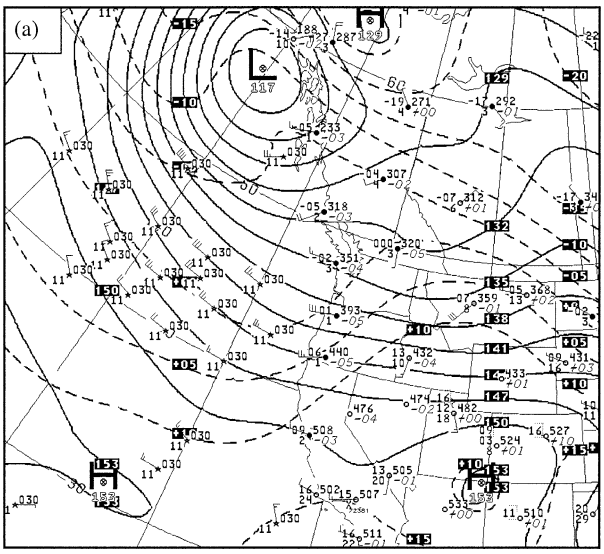

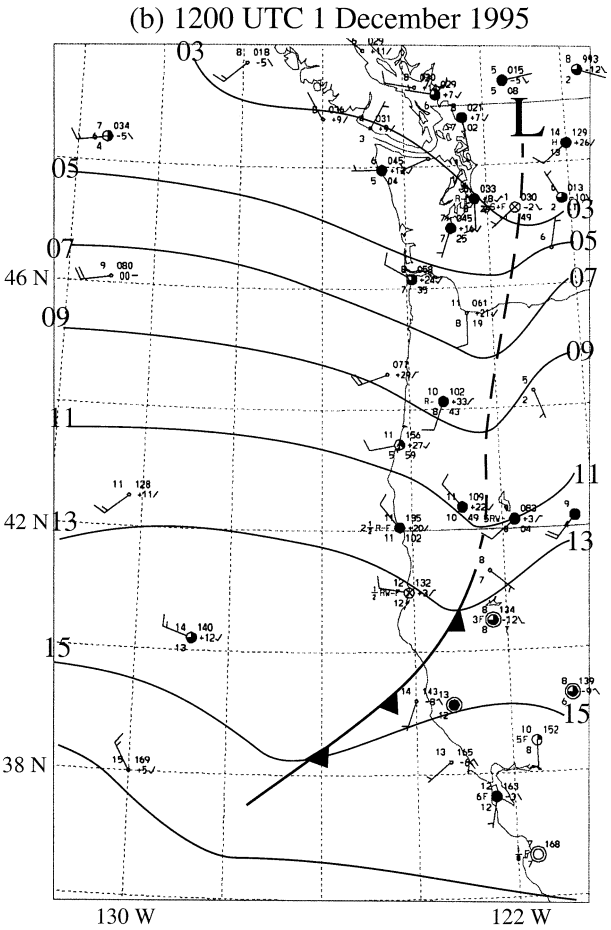

FIG. 4. (a) Same as in Fig. 1b except at 1200 UTC 1 December 1995. (b) Same as in Fig. 3 except at 1200 UTC 1 December 1995.

FIG. 4. (*Continued*)

idation (Fig. 5).[2] At 0515 UTC 1 December (Fig. 5a), the surface trough was located near the southern Oregon coast in a zone of weak confluence between 20–24 m s^{-1} south-southwesterlies adjacent to the Oregon coastal terrain and the weaker 10–15 m s^{-1} southwesterlies farther offshore and to the north along the coast. A broken area of light-to-moderate precipitation was located within this confluent wind transition at this time.

By 0642 UTC 1 December (Fig. 5b), the cyclonic wind shift across the trough had sharpened, with an abrupt wind shift across the front from ~24–26 m s^{-1} southwesterlies near the coast to 5–10 m s^{-1} westerlies farther offshore. A surface time series at buoy 44027 revealed this trough southwest of the coast was also associated with a more significant temperature gradient (cf. Fig. 5 of YS), offering further evidence that the frontal wind shift and temperature gradient had intensified during the preceding 6 h. Yu and Smull (2000) suggested that this rapid enhancement of low-level convergence along the front supported the rapid development of a narrow but intense rainband, in which observed radar reflectivities that reached 40 dBZ near the coast diminished somewhat with distance offshore. Another broken rainband and zone of winds veering from southerly to southwesterly flow was located along the Oregon coast to the south of the front.

The National Weather Service Weather Surveillance Radar 1988-Doppler (WSR-88D) S-band radar (BHX) on Cape Mendocino (hereafter abbreviated as CM) provides more continuous, larger-scale perspective to the precipitation evolution of this landfalling frontal system following this period of rapid frontal intensification documented by the NOAA P-3 aircraft off the Oregon coast. Figure 6 shows two selected radar reflectivity images for the 0.5° elevation scan as the coastal precipitation evolved. At 0730 UTC 1 December (Fig. 6a), the NCFR along the front near the coast (labeled A) extended southwest of the Oregon–California border. A secondary prefrontal rainband (B) had a more north–south orientation and was located east of band A, approximately 50 km upstream of CM. The leading edge of band B was sharply defined, with little or no precipitation to its east. This narrow region with no precipitation had an orientation that roughly conformed to the shape of the coastline at this time.

During the next 2 h precipitation band B moved inland, and was located over CM at 0930 UTC (Fig. 6b). Meanwhile, the precipitation along the front to the north had weakened and become less organized, a trend also noted by YS (cf. their Figs. 13, 16). In this region they showed that there was less low-level convergence since the flow near the coast was more southwesterly (i.e., less blocked) than observed 2 h earlier, and the terrain-enhanced flow had decreased to 20–22 m s^{-1}.

[2] YS provide a detailed description of how the dual-Doppler synthesis was completed. Also, see YS for more details on the mesoscale structures observed during this event.

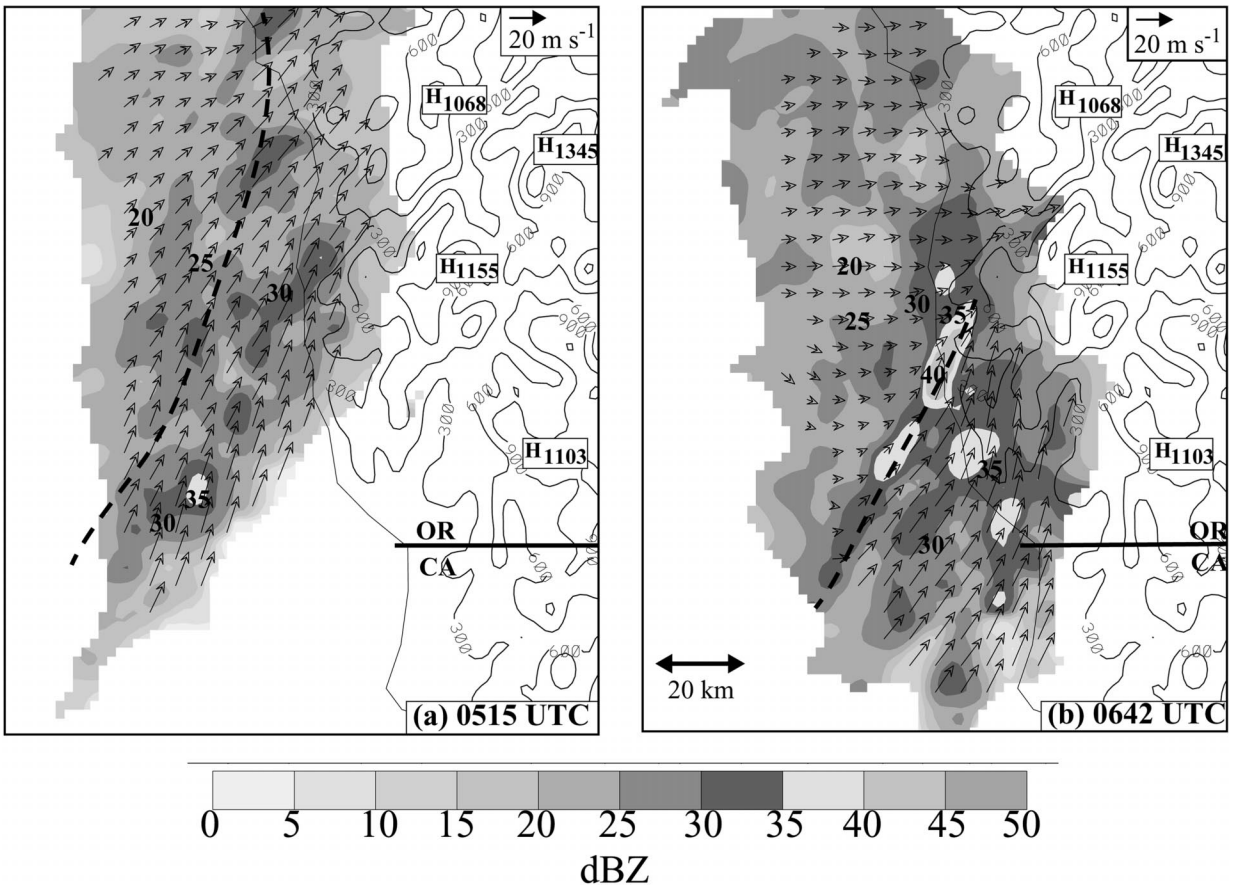

FIG. 5. Observed ground-relative winds (vectors, key at upper right) and radar reflectivity (dBZ, shading) at 1000 m MSL derived from P-3 airborne Doppler analyses valid at (a) 0515 and (b) 0642 UTC 1 Dec 1995. Solid contours represent terrain height at 300-m interval. A bold straight line denotes the location of the California–Oregon border (CA–OR), and the bold dashed line represents the frontal position as determined by the winds and precipitation. The box drawn in Fig. 3 indicates the location of this analysis domain relative to the larger-scale analysis.

4. Model simulation of COAST IOP8

a. Model description

The Penn State–NCAR MM5 (version 2.12) was used in nonhydrostatic mode to simulate this case and to provide additional data for diagnosing the frontal interaction with the coastal mountains. For this simulation, stationary 3- and 9-km domains were nested within a 27-km domain using one-way interfaces (Fig. 7a). The model top was set at 100 mb. Thirty-three unevenly spaced full-sigma levels were used in the vertical, with the maximum resolution in the boundary layer.[3] Five-minute-averaged terrain data were analyzed to the 27- and 9-km model grids using a Cressman analysis scheme and filtered by a two-pass smoother/desmoother. For the 3-km domain, a 30″ topography dataset was interpolated to the grid in order to better resolve the coastal mountains (Fig. 7b). A 10′ land use dataset from NCAR was used to initialize the various surface categories for all domains; however, the coastlines in the 9- and 3-km domains were improved by setting grid points to either coniferous forest or water when the 30″ topography at those grid point is greater than or equal to zero, respectively. Initial atmospheric conditions and sea surface temperatures were generated at 1200 UTC 30 November 1995 for the 27-, 9-, and 3-km domains by first interpolating the National Centers for Environmental Prediction (NCEP) global analyses (2.5° latitude–longitude resolution) to the model grid. These analyses were improved by incorporating surface and upper air observations using a Cressman-type analysis scheme (Benjamin and Seaman 1985). Additional analyses generated in the same manner were linearly interpolated in time every 12 h in order to provide the evolving lateral boundary conditions for the 27-km domain. These analyses were also used to apply four-dimensional data assimilation (FDDA) on the 27-km domain during the first 6 h of the integration of all simulations in order to obtain

[3] The 33 full-sigma levels were σ = 1.0, 0.99, 0.98, 0.97, 0.96, 0.94, 0.92, 0.90, 0.88, 0.86, 0.83, 0.80, 0.77, 0.74, 0.71, 0.68, 0.64, 0.60, 0.56, 0.52, 0.48, 0.44, 0.40, 0.36, 0.32, 0.28, 0.24, 0.20, 0.16, 0.12, 0.08, 0.04, 0.0.

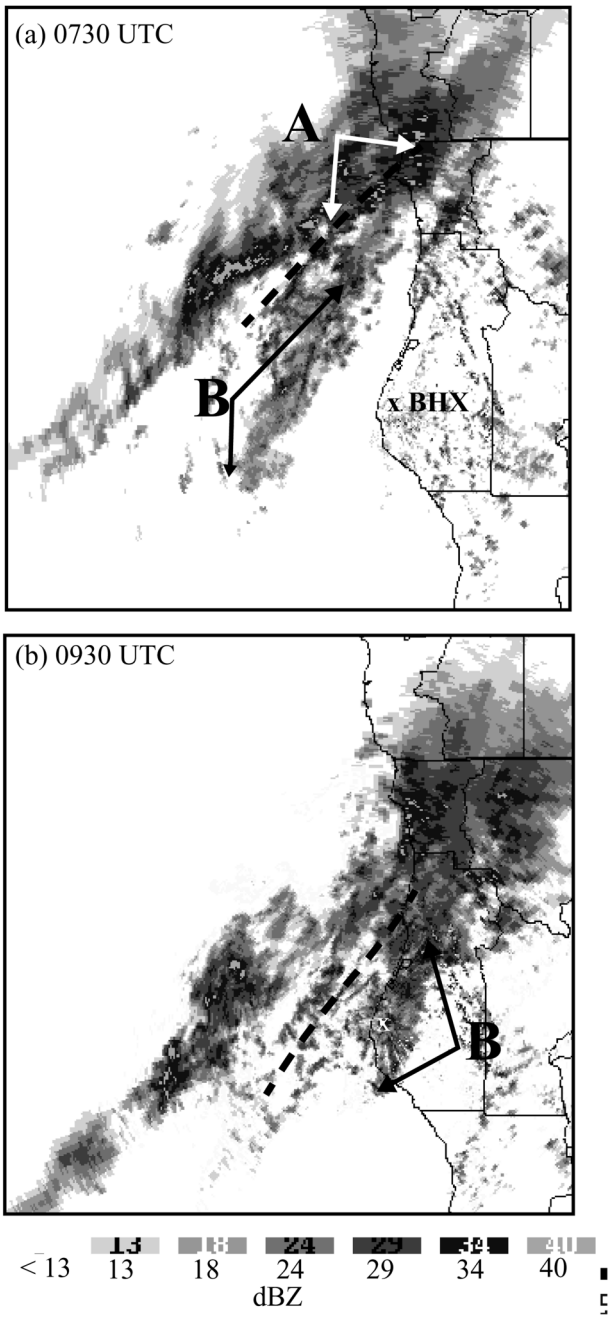

FIG. 6. Base scan (0.5° elevation) PPI display of radar reflectivity (dBZ) from the Eureka WSR-88D radar (BHX) at (a) 0730 and (b) 0930 UTC 1 Dec 1995. Rainbands A and B are indicated by the arrow positions. Frontal position is indicated by the dashed lines and are derived using observations shown in YS.

a more realistic simulation.[4] Specifically, winds and moisture within the planetary boundary layer (PBL) and the temperature, winds, and moisture above the PBL were nudged toward the NCEP analyses.

The control (CTL) simulation used the explicit moisture scheme of Reisner et al. (1998), which includes prognostic equations for cloud ice and water, snow, rain, and graupel. The Kain–Fritsch cumulus parameterization (Kain and Fritsch 1990) was applied, except for the inner domain where convective processes could be resolved explicitly. The PBL was parameterized using the scheme of Zhang and Anthes (1982). Klemp and Durran's (1983) upper-radiative boundary condition was applied in order to prevent gravity waves from being reflected off the model top.

b. Frontal interaction with steep coastal terrain

Figure 7a shows sea level pressure, 950-mb temperature, and surface winds in the 12-h simulation valid at 0000 UTC 1 December 1995 (12 h) for the 27-km CTL simulation. As observed (Fig. 1c), a surface trough extended southward from near Vancouver Island southward a few hundred kilometers offshore of the Washington and Oregon coast. Off the California coast, this trough extended southwestward as a weak cold front and was associated with a more significant airmass transition and wind shift. The weakness in the north–south sea level pressure gradient along the trough offshore of Vancouver Island is suggestive of the disturbance L_1 noted in the observations.

The evolving MM5 wind, temperature, and sea level pressure along the U.S. west coast was verified using the time series at those stations considered by YS (cf. their Figs. 1, 5). For convenience the coastal observations are shown again (Fig. 8a) in conjunction with the corresponding MM5 forecast values (Fig. 8b). The model data were objectively analyzed to each station using the hourly data from the highest-resolution domain a station was located within. The 40-m model winds were reduced to 10 m using a logarithmic profile. Overall, the MM5 captured many of the salient attributes of this event, such as a sharper frontal wind shift adjacent to the steep California coastal terrain (buoys 46027 and 46030) as compared to more northern coastal stations. The surface expression of the prefrontal terrain-enhanced flow in the model at buoy 46027 (13 m s^{-1}) was within 1–2 m s^{-1} of that observed; however, the model buoy 46027 winds were more southwesterly, thus exhibiting a larger cross-barrier component than observed. The timing of trough passage was generally well simulated along the coast; however, the amplitudes of the landfalling trough and postfrontal ridging in the model were 1–3 mb less than was observed. The model developed an anomalous secondary trough in the cold air along the California coast, which resulted in a temporary wind shift back to southwesterly flow. This difference, however, had no obvious impact on simulated structural details in the prefrontal regime or the front itself.

[4] The FDDA scheme applies Newtonian relaxation to nudge the model toward the reanalyzed NCEP 3-h surface and 12-h upper-air gridded analyses (Stauffer and Seaman 1990; Stauffer et al. 1991). Only a 6-h period of nudging was used in order to allow time for the model to independently develop coherent mesoscale structures during the IOP period.

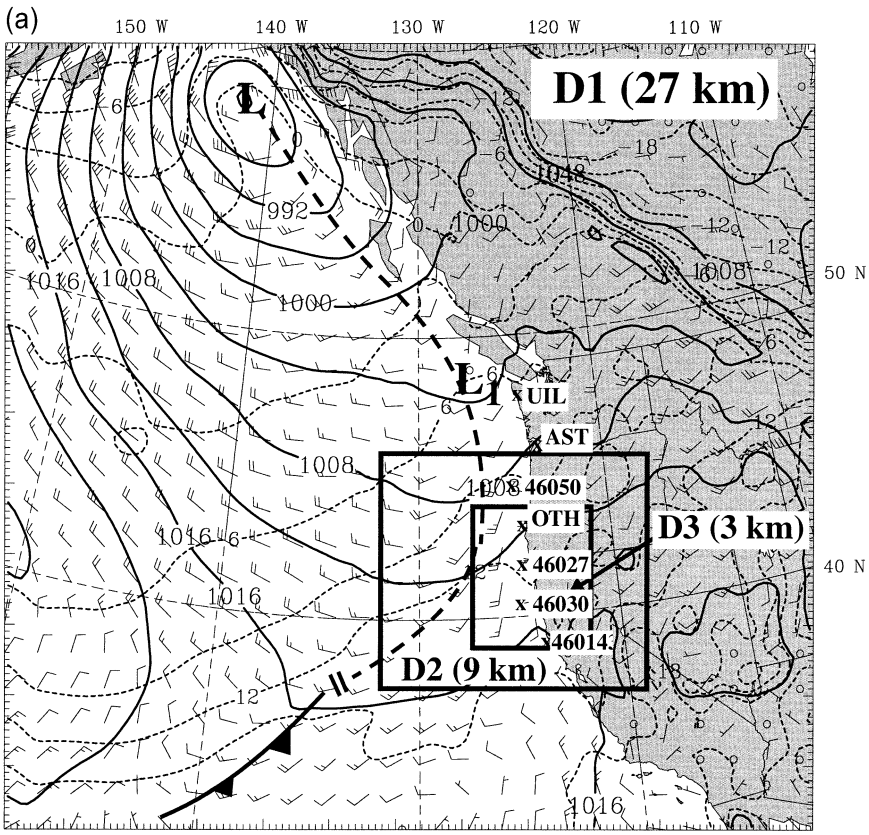

FIG. 7. (a) Sea level pressure (solid) every 4 mb, 950-mb temperatures (dashed) every 3°C, and surface wind barbs (full barb = 10 kt) at 0000 UTC 1 Dec 1995 (12 h) for the 27-km simulation. The inner boxes (D2 and D3) show the location of the 9- and 3-km nested domains. The Xs show the observation stations used in the time series in Fig. 8, and the tick marks along the margin are 27 km apart. (b) Model terrain contoured every 300 m for the 3-km domain. Terrain heights of 700–1000 m and greater than 1000 m are shaded light and dark gray, respectively. Line segments AA′, BB′, CC′, and DD′ are the locations for the cross sections for Figs. 13, 14, and 19. The small tick marks along the margin are 3 km apart.

Figure 9 shows the horizontal evolution of the simulated surface winds, temperatures, and reflectivities for a portion of the 9-km grid-spacing domain at 0300 and 0600 UTC 1 December (i.e., 15- and 18-h forecasts).[5] At 0300 UTC (Fig. 9a), there is weak veering from southerly to south-southwesterly flow northward along the coast across a developing trough and a broken line of precipitation associated with the low-level baroclinicity off the southern Oregon coast. The strongest wind and temperature transitions were offshore of the California coast to the south of 41°N, and this was where the most intense area of precipitation was simulated at the surface. Along the coast, significant low-level warm advection was associated with the advancing thermal ridge. By 0600 UTC (Fig. 9b), a clearly defined precipitation band had developed along an intensifying wind shift and temperature transition near the Oregon–California border. The heaviest model precipitation (>35 dBZ) along the developing surface front extended about 75 km offshore, with a local maximum (42 dBZ) over the coastal range. Compared with the observations at this time (Fig. 3), the simulated surface trough is approximately 50 km east of the observed position (i.e., slightly too fast), and the simulated wind shift immediately off the southern Oregon coast is less sharp than was observed).

The 3-km domain illustrates the detailed structural evolution of the front as it rapidly intensified and moved southward along the northern California coast (Fig. 10). At 0500 UTC 1 December (Fig. 10a), the developing trough was associated with weak confluent flow between ~13 m s^{-1} terrain-parallel southerlies along the coast and ~8 m s^{-1} southwesterlies offshore. Several broken areas of light to moderate precipitation extended from southwest to northeast near this wind transition.

During the next 2 h the simulated mesoscale evolution is qualitatively similar to that observed by the NOAA P-3 aircraft and Eureka WSR-88D radars (cf. Figs. 5,

[5] The model-based reflectivities were calculated using empirical relations based on the model cloud and precipitation mixing ratios (Fovell and Ogura 1988).

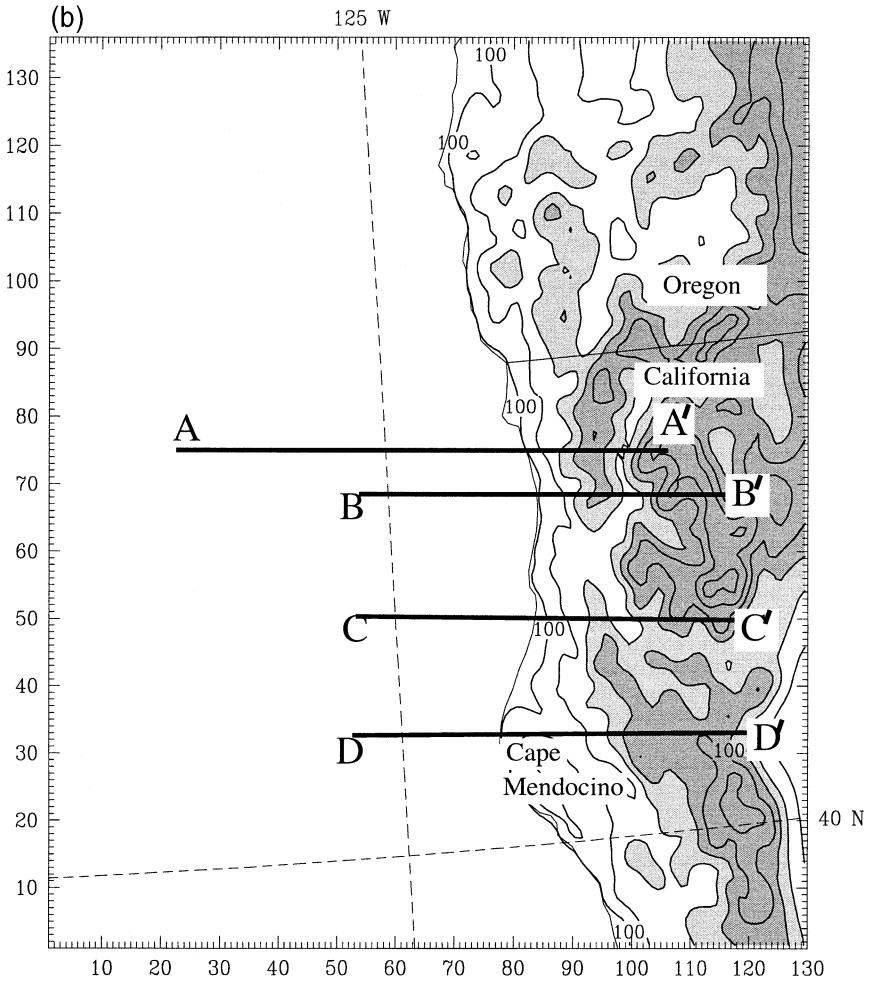

FIG. 7. (*Continued*)

6). By 0700 UTC (Fig. 10b), the frontal precipitation band, temperature gradient, and wind shift had intensified further, with the southerly prefrontal flow along the northern California coast increasing to 15 m s^{-1} and the surface winds veering from southerly to west-southwesterly across the front. The maximum model reflectivities (>35 dBZ) and wind shift along the front are suggestive of a classical NCFR structure confined to a zone within approximately 200 km of the coast. Another larger banded area of precipitation to the northwest of the front is suggestive of a wide, cold frontal rainband, while a prefrontal rainband was associated with a weak wind transition from southerly to south-southwesterly flow. This simulated prefrontal band was orientated more northeast to southwest than its observed counterpart, which may be the result of the model underestimating the blocking and the terrain-enhanced flow strength (cf. Fig. 8).

By 0900 UTC (Fig. 10c), widespread prefrontal precipitation had reached the coast near CM, but was no longer so well organized. As in the observations (Fig. 6b), the heaviest banded precipitation was associated with the NCFR near the coast and over the coastal mountains, where locally there was a rapid wind shift from southwesterly to westerly flow. This area of banded precipitation was more broad and intense over the nearshore coastal mountains, evidently as a result of the superposition of the orographic and frontal modes of precipitation. As observed (cf. Fig. 5b), during the next 2 h the simulated wind shift and NCFR continued to weaken as the front moved southeastward toward CM. The simulated frontal movement down the coast continued to be somewhat (~1–2 h) slower than observed, consistent with the weaker simulated postfrontal northwesterlies (Fig. 8). By 1100 UTC (cf. Fig. 10d), which corresponds with the observed 0930 UTC frontal position (Fig. 6b), there was only a broad area of moderate precipitation along the front, and the surface southerlies ahead of the front along the coast were 2–5 m s^{-1} weaker than at 0900 UTC.

As the thermal gradients, wind shift, and precipitation structures intensified and moved southward along the coast at low levels, they developed some ''nonclassical'' structures. Figure 11 shows the evolution of the 3-km

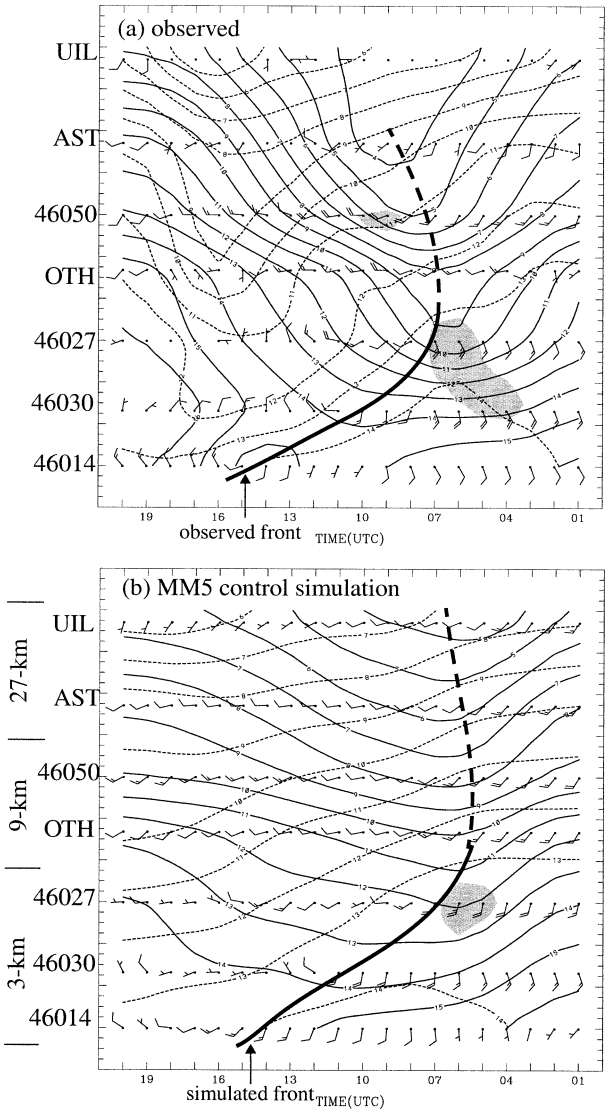

FIG. 8. Objectively analyzed (a) observed (from YS their Fig. 5) and (b) simulated time section of hourly surface winds (winds greater than 10 m s^{-1} are shaded), sea level pressure (solid every I mb), and surface temperatures (dashed every 1°C) for selected stations along the Pacific Northwest coast at 0100–2000 UTC 1 Dec 1995. Locations for the surface stations are shown in Fig. 7a.

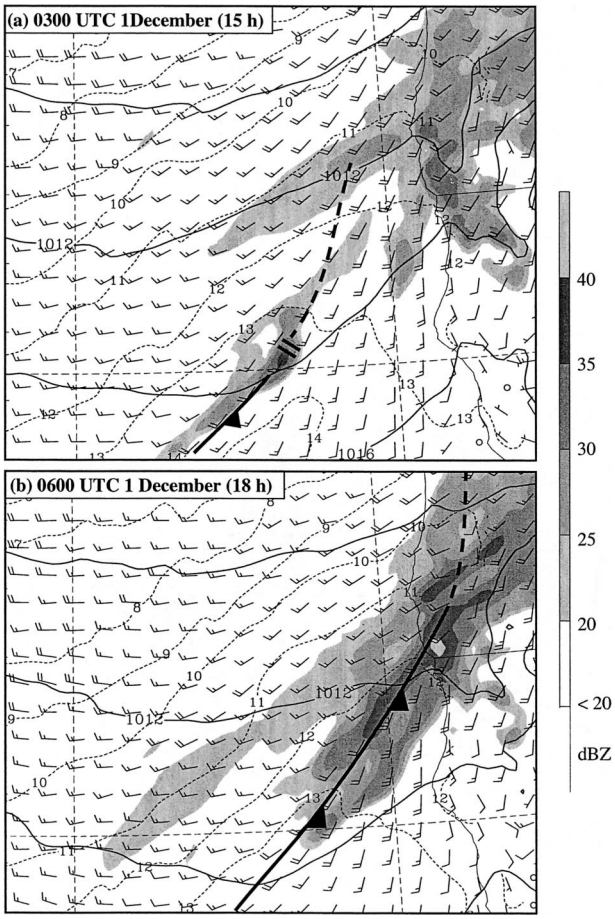

FIG. 9. Model surface analysis for a portion of the 9-km domain at (a) 0300 UTC 1 Dec (15 h) and (b) 0600 UTC 1 Dec (18 h) showing sea level pressure (solid) every 2 mb, winds at 30 m above the surface (1 full barb = 10 kt), 500-m temperatures (dashed) every 1°C, and model reflectivities (shaded).

thermal, wind, and reflectivity structures at 850 mb (near crest level). At 0700 UTC (Fig. 11a), the thermal ridge at 850 mb was situated along the coast and the leading (southern) precipitation band had intensified along the leading edge of cold advection at 850 mb, which was located 20–30 km *ahead* of the surface front at this time (Fig. 10b). There was a weak 3 m s^{-1} wind speed difference across this leading precipitation band at 850 mb but little wind direction shift. By 1100 UTC (Fig. 11b), the front at 850 mb had moved inland in concert with the leading edge of the precipitation shield, and this 850-mb transition was located 30–40 km *ahead* of the surface front at this time (cf. Fig. 10d).

c. Coastal flow development and interaction with the landfalling front

One of the key features noted by YS for this event was the development of terrain-enhanced flow immediately upstream of the steep coastal terrain, and its interaction with the landfalling front along the northern California coast. In order to illustrate the evolution of the low-level winds along the northern California coast, Fig. 12 shows the 3-km domain winds and pressures at 0.3 and 0.8 km ASL for 0600, 0800, and 1000 UTC 1 December 1995. In comparison to the 0.75-km airborne Doppler radar observations shown in YS, the model underestimated the strength of the low-level coastal flow at intermediate observed times (0647 UTC) by as much as 5–7 m s^{-1} and 1–2 m s^{-1} at 0843 UTC.[6] These model wind speed errors are related to low-level stability dif-

[6] Because of model timing/position error, the 0600 and 1000 UTC forecasts can be meaningfully compared with 0647 and 0843 UTC observational analyses, respectively.

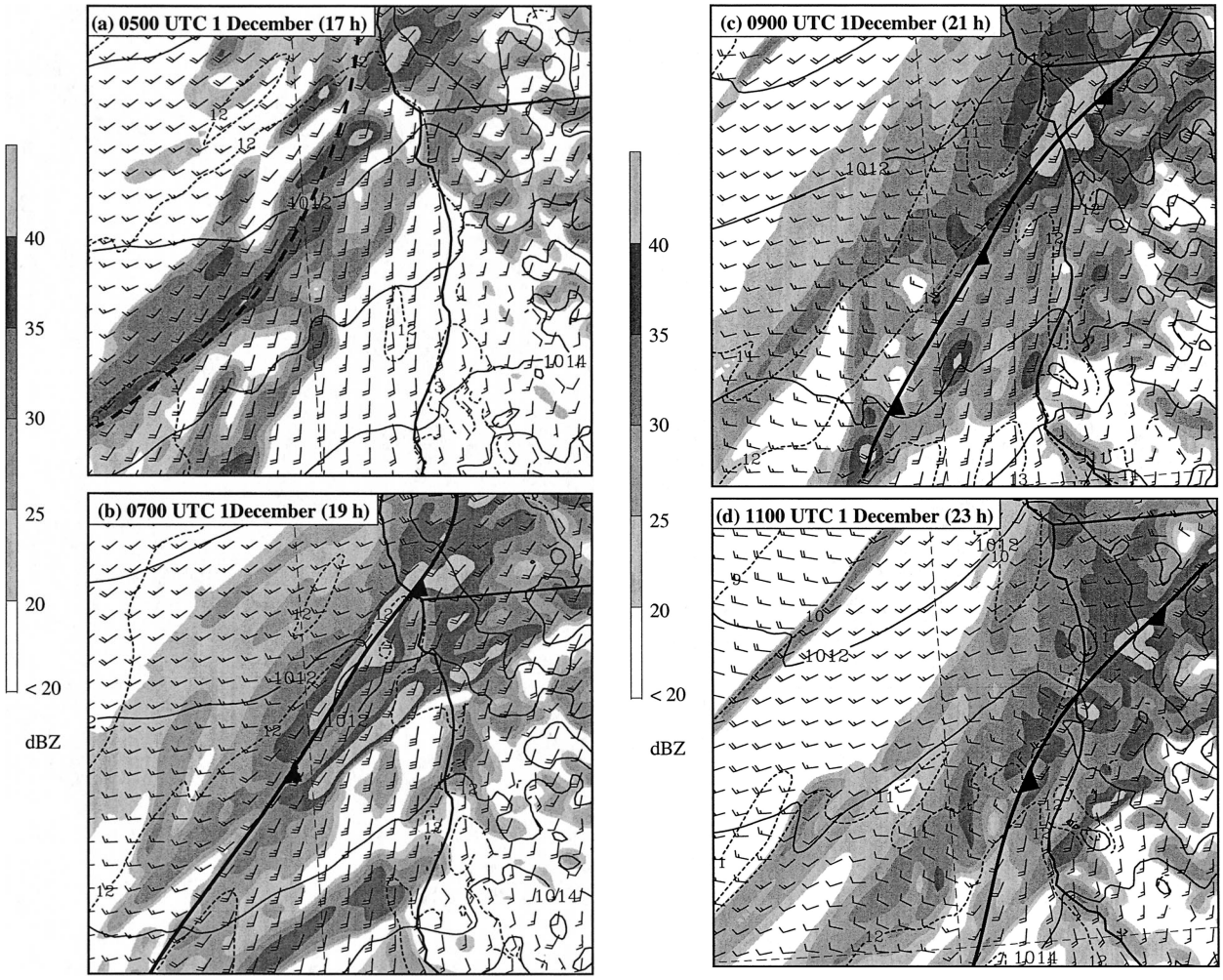

FIG. 10. Model surface analysis for a portion of the 3-km domain at (a) 0500 (17 h), (b) 0700 (19 h), (c) 0900 (21 h), and (d) 1100 UTC 1 Dec (23 h) showing sea level pressure (solid) every 1 mb, winds at 30 m above the surface (1 full barb = 10 kt), 500-m temperatures (dashed) every 1°C, and model reflectivities (shaded).

ferences with respect to the stratification actually observed. For example, at 0300 UTC 1 December, the 850-mb modeled southwesterly winds are 14 m s^{-1} a few hundred kilometers upstream of the coast (not shown), in reasonable agreement with observed values (cf. Fig. 1b). In contrast, the simulated moist static stability in the surface–850-mb layer ($N_m \sim 7.5 \times 10^{-3}$ s^{-1}) is 30% weaker than estimated on the basis of in situ P-3 observations in this region (cf. Fig. 7 of YS). As a result, the prefrontal Froude number (Fr) in the model averaged in the 0.1–1.5 km MSL layer was ~1.1 immediately upstream of the California–Oregon border (where the moist $N_m \sim 7.5 \times 10^{-3}$ s^{-1}, $h_m \sim 1400$ m, and $U \sim 12$ m s^{-1}), compared to Fr ~ 0.8 in the observations (YS, p. 1591). A larger Froude number in the simulation corresponds to a reduced propensity for terrain blocking and resulted in weaker terrain-enhanced flow near the California–Oregon border in the simulation. Meanwhile, farther south along the coast in a 150-km swath north of CM, the model N_m and Fr were 1.5×10^{-2} s^{-1} and 0.6, respectively. This higher stability was associated with cooler and drier air originating over CM (Fig. 12). The more accurate prediction of stratification to the south resulted in more accurate coastal winds being simulated at later times as the front sagged southward between 0800 and 1000 UTC.

The 3-km model simulation also illuminates the wind evolution within regions along the coast that were not observed by the NOAA P-3. At 0600 UTC (Figs. 12a,b), the 0.3-km model wind speeds are highly variable in the north–south direction along the northern California coast. A narrow plume of relatively weak flow (<10 m s^{-1}) is situated just north of CM, and the winds gradually accelerate to 15 m s^{-1} 100 km to the north in a region where the along-barrier pressure gradient is enhanced. This illustrates that the concave coastline geometry around CM resulted in lower-momentum air being advected over downstream coastal

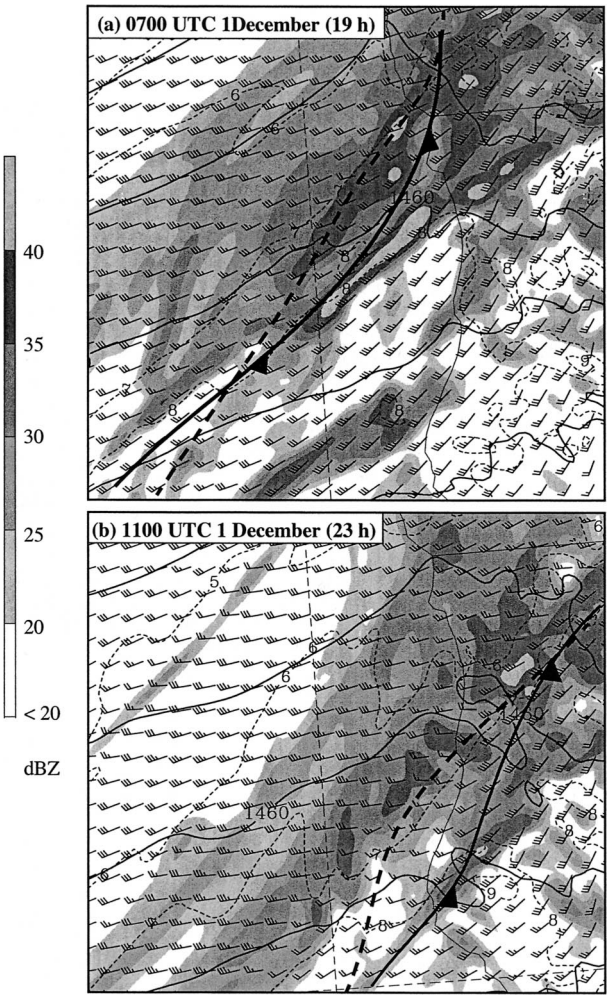

FIG. 11. Model 850-mb analysis for a portion of the 3-km domain at (a) 0700 (19 h) and (b) 1100 UTC 1 Dec (23 h) showing geopotential heights (solid) every 10 m, winds (1 full barb = 10 kt), temperatures (dashed) every 1°C, model reflectivities (shaded), and 850-mb front. The surface front is indicated by the bold dashed line.

waters. As a result, the strongest low-level winds were situated 25 km offshore and well to the north of CM. In contrast, at 0.3 km MSL to the north near the Oregon–California border, the north–south-orientated flow was adjacent to the relatively steeper and more two-dimensional terrain. At 0.80 km MSL (Fig. 12b), the south-southwesterly flow accelerates from 15 to 20 m s^{-1} as it approaches the coast. Significant accelerations also occur just inland at 0.80 km since there is a strong northeastward-directed pressure gradient adjacent to the Klamath Mountains. At this time the frontal position was oriented from northeast to southwest and there was little change with height.

At 0800 UTC (Figs. 12c,d), the areal coverage of strong winds increased as pressure gradients tightened ahead of the front along the coast. The winds at 0.3 km MSL were more southwesterly upstream of CM, which resulted in less offshore flow to the north of CM and stronger winds closer to the coast than at 0600 UTC. The southward progression of the low-level front at this time was being slowed by blocking effects, which resulted in a bend of the front near the coast. By 1000 UTC (Figs. 12e,f), the front displayed an unusual convex-westward orientation along the coast, and the front at 0.8 km MSL was approximately 20 km west of its position at 0.3 km. As the front sagged south the strength and areal coverage of the terrain-enhanced flow also weakened.

To document further the evolving vertical structure of the simulated front as it approached the coast, Fig. 13 shows a cross section (AA′) normal to the northern California coastal terrain. At 0500 UTC 1 December (Fig. 13a), the frontal temperature gradients were relatively weak (particularly in the surface layer) and focused approximately 60 km offshore, where there was a narrow band of moderate (35 dBZ) precipitation along the front. Meanwhile, along the coastal mountains there was an enhancement in the terrain-parallel winds (~17 m s^{-1}), and the slight upward tilt of the isentropes near the coast is indicative of the low-level cool air partially blocked by the barrier. By 0700 UTC (Fig. 13b), the terrain-parallel winds increased to 20 m s^{-1} over the higher windward slopes. As the front approached, precipitation intensity in this zone increased to 40 dBZ, and the low-level frontal temperature and wind speed gradients also increased significantly. Another intense precipitation area had developed over the lower windward slope during the past 2 h, and the ascent of flow over the orographically induced cold dome near the coast resulted in an extension of this orographic precipitation enhancement approximately 10 km offshore. By 0900 UTC (Fig. 13c), the superposition of the frontal vertical motions and the upslope flow over the lower windward slope created a wider area of enhanced precipitation than 2 h earlier. The wind speed and temperature gradients also continued to increase, as the front merged with the terrain-enhanced flow. During the next 2 h as the front ascended the windward slope (Fig. 13d), the associated precipitation and wind shift weakened; however, the low-level temperature gradient below 750 mb did not decrease as the front moved over the first rise in coastal terrain.

The northern California coastal topography falls and thus becomes less steep to the south, especially approaching CM (Fig. 7b); therefore, Fig. 14 shows a series of west–east cross sections to illustrate how the landfalling frontal temperature, wind, and precipitation structures evolved in the presence of this variable terrain. As the front approached the steep coastal topography across section BB′ (Fig. 14a), there was simulated 19 m s^{-1} terrain-enhanced flow and an intense NCFR near the coast. For section CC′ (Fig. 14b), the low-level coastal flow weakened to 15 m s^{-1} and the maximum retreated up the windward slope, and the frontal circulations and associated precipitation began to attenuate. Finally, as the front neared the coast across section

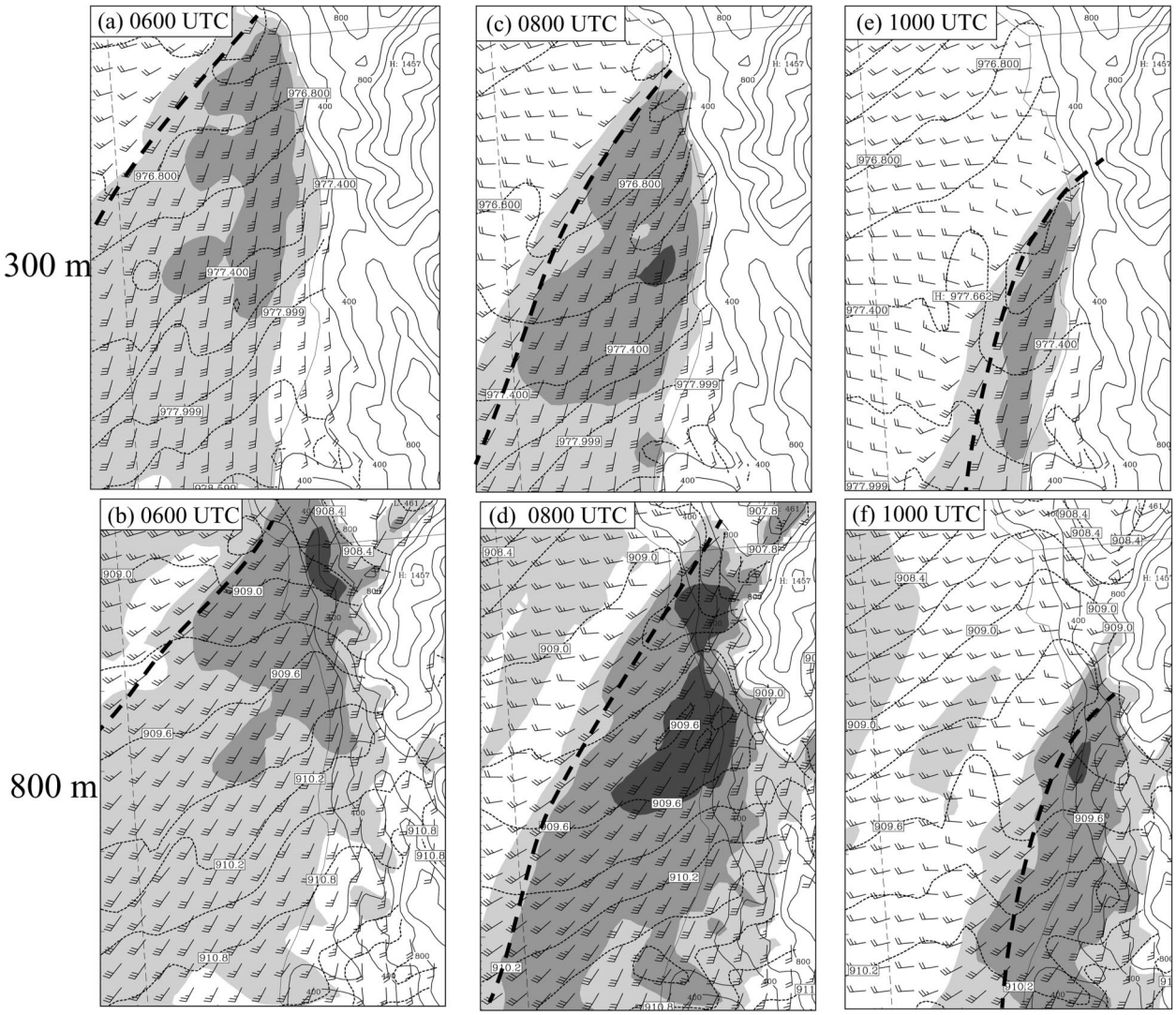

FIG. 12. The 3-km model winds (full barb = 10 kt) and pressures (dashed every 0.3 mb) at (a) 300 and (b) 800 m MSL for 0600 UTC 1 December 1995. (c) and (d) Same as in (a) and (b) except at 0800 UTC. (e) and (f) Same as in (a) and (b) except at 1000 UTC. Wind speeds greater than 13, 16, and 19 m s^{-1} are shaded light, medium, and dark gray, respectively. The frontal position is dashed.

DD′ (Fig. 14c), the cross-shore transition in meridional wind between the front (-3 m s^{-1}) and the terrain-enhanced flow (to 14 m s^{-1}) had weakened and tilted upward to the east more with height than a few hours earlier, and there was no organized precipitation at the front. Overall, these results are consistent with the observationally based findings of YS, which suggest that the lower coastal topography to the south contributed to the rapid weakening of the frontal circulation and precipitation.

5. Discussion and additional experiments

An important objective of this study is to determine the mechanism(s) responsible for the rapid intensification of the front and associated precipitation features as they approached the steep coastal topography, as well as the subsequent weakening of the NCFR as the front made landfall farther to the south. Yu and Smull (2000) examined the possible terrain contributions to the precipitation enhancement in the coastal zone, but the MM5 simulations discussed herein allow us to separate the relative contributions of the large-scale forcing, terrain, and diabatic effects to this development.

a. Evaluation of large-scale influences

To investigate the relationship between the synoptic-scale forcing and rapid spinup of precipitation near the coast, our analysis of the control (CTL) model simulation begins by quantitatively solving the quasigeostrophic (QG) omega equation. The following methods applied to the 27-km model domain resemble those described in Stoelinga et al. (2000). First, the height

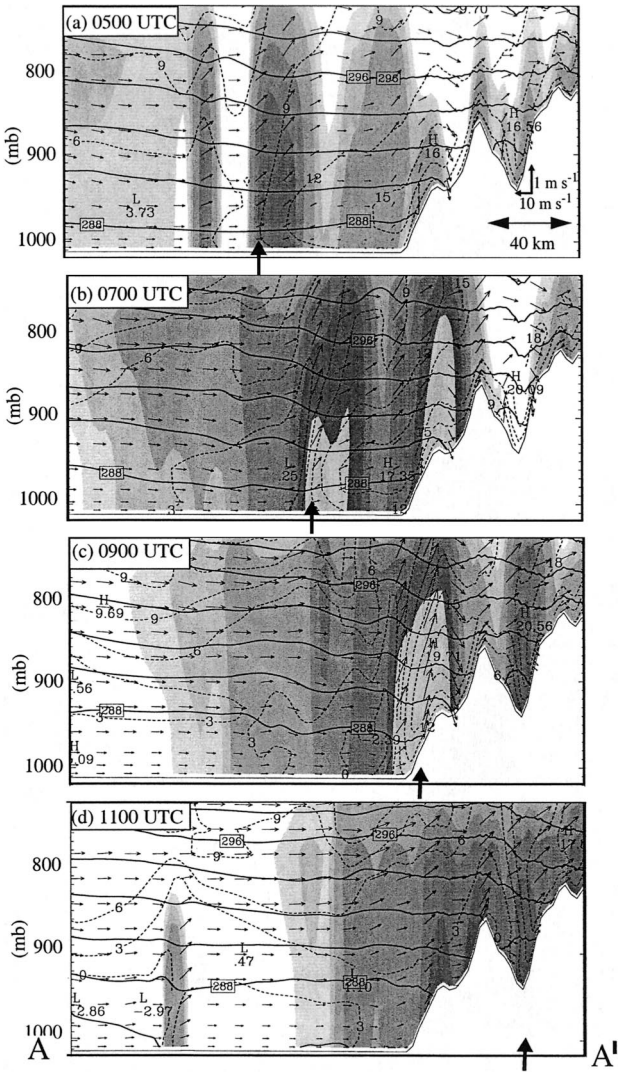

FIG. 13. Cross section AA′ for the 3-km domain at (a) 0500, (b) 0700, (c) 0900, and (d) 1100 UTC 1 Dec 1995 showing potential temperature (solid every 2 K), model reflectivities (shaded using key in Fig. 11), north–south wind component (dashed every 3 m s^{-1}), and the total circulation (vectors) in the cross section. The surface front is indicated by the bold arrow. The locations of the cross sections are shown in Fig. 7b.

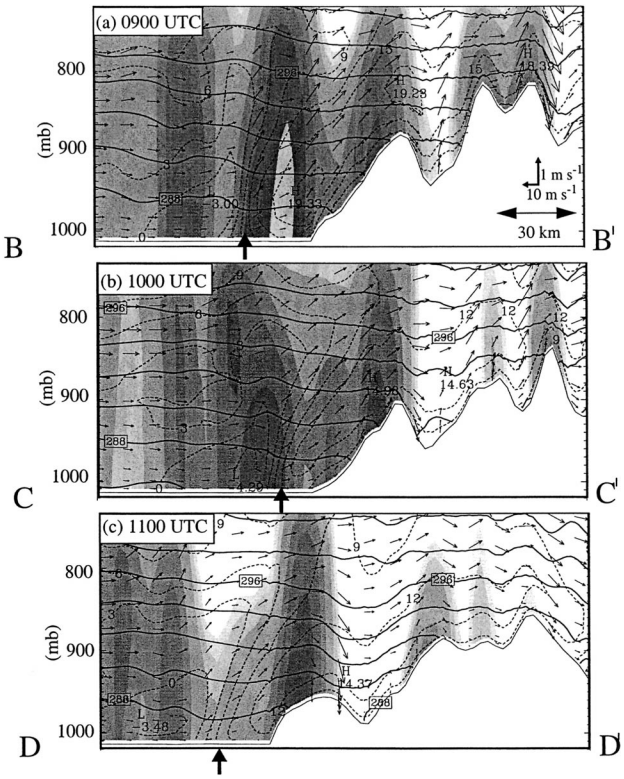

FIG. 14. Cross sections (a) BB′, (b) CC′, and (c) DD′ for the 3-km domain at (a) 0900, (b) 1000, and (c) 1100 UTC 1 Dec 1995 showing potential temperature (solid every 2 K), model reflectivities (shaded using key in Fig. 11), north–south wind component averaged for either side (north–south) of the cross section (dashed every 3 m s^{-1}), and circulation vectors in the cross section. The surface frontal position is shown by the bold arrow. The locations of the cross sections are shown in Fig. 7b.

and temperature fields were interpolated from the model's sigma levels to pressure levels with a vertical grid spacing of 30 mb. Because the area of interest includes substantial topography, a step lower boundary was defined such that the lowest grid point in each column is the lowest above-ground point. A low-pass filter was applied to the temperature and height fields to remove small-scale variability that is not consistent with QG scaling. The low-pass filter was set to attenuate wavelengths of 300 km by 50%, similar to that suggested by Barnes et al. (1996) and Stoelinga et al. (2000). The Q-vector form of the omega equation was evaluated using these smoothed fields, and a relaxation method was used to invert the equation to obtain the vertical velocities. The upper boundary condition was defined as zero vertical velocity at 100 mb, and an Ekman and topographic lower boundary condition was used as defined in Hoskins et al. (1978) and Stoelinga et al. (2000).

At 0000 UTC 1 December (Fig. 15a), the QG-forced ascent in the layer between 700 and 500 mb was 1–2 dPa s^{-1} over a broad area of the eastern Pacific. This ascent corresponds roughly with the region of mid- to upper-level cloudiness observed at this time (cf. Fig. 2a). During the next 8 h the QG-forced ascent nearly tripled in magnitude adjacent to the northern California coast (Fig. 15b) as a result of the increased flow curvature and differential vorticity advection ahead of the approaching upper-level trough. A simulation without the coastal terrain (see the next section for details) suggests that most of this increase in upper-level forcing was not related to the coastal topography (i.e., QG forcing still doubled even in the absence of coastal topography); although, the larger Rocky Mountains farther inland may have played an important role.

Overall, these results suggest that the increased large-

scale forcing was favorable for the development of the coastal precipitation during this period. Specifically, the amplifying ageostrophic circulations associated with the large-scale forcing released potential instability as the low-level atmosphere became saturated. Obviously, the increased large-scale forcing cannot explain the mesoscale banded nature of precipitation; therefore, the roles of terrain and diabatic influences are explored in the following sections.

b. No coastal terrain (NCST) simulation

In order to further investigate the interaction between the landfalling front and the coastal topography, a separate experiment (with no coastal terrain, NCST) was conducted in which the steep coastal terrain was removed in northern California. For this NCST run, the model configuration was identical to that in CTL except that the coastal terrain over a selected area was removed in all three domains and replaced by flat land (Fig. 16). Since theory holds that terrain-blocking effects may extend upstream over a Rossby radius, the terrain was removed as far as 200 km inland from the coast to eliminate most of the blocking-induced flow perturbations.

As shown in Fig. 17a, valid at 0700 UTC 1 December, even in the absence of steep coastal terrain a broad band of moderate precipitation developed along the front; however, there were no narrow bands of intense (>40 dBZ) precipitation near the front as in the CTL run (cf. Figs. 10b,c). The prefrontal surface winds in the NCST run were 3–5 m s^{-1} weaker and more southwesterly near the coast than the CTL. The large-scale QG forcing for the NCST (not shown) was within 10%–20% of that in the CTL simulation, which suggests that the increased low-level convergence associated with the terrain-enhanced flow in the CTL was pivotal in organizing and intensifying the frontal precipitation, particularly within 100 km of the coast, thus supporting a hypothesis advanced by YS. However, since a notable increase in areal coverage of precipitation occurred even in the absence of steep coastal terrain, large-scale forcing apparently also contributed to this coastal development. Yet another simulation was conducted in which the flat land was replaced by water (not shown), and no further weakening of the precipitation band and frontal wind shift occurred. This suggests that differential friction effects, as previously emphasized by Doyle (1997), were not especially important in enhancing the precipitation along the coastal zone in the present case. The frontal position along the coast at 0700 UTC 1 December was located at a position similar to that seen nearly 2 h later in the CTL run, which convincingly illustrates that the southerly terrain-enhanced flow acted to significantly retard the front's forward progression.

By 0900 UTC 1 December (Fig. 17b), when the frontal had advanced into a zone of less-pronounced coastal terrain, the wind and precipitation structures in the NCST were more similar to those in the CTL at 1100 UTC 1 December (cf. Fig. 10d). The frontal precipitation in the CTL had weakened more dramatically than the NCST during the past few hours. MM5 simulations suggest that large-scale forcing did not decrease during this time (not shown); however, for the CTL there was a reduction in the terrain-enhanced flow by the lower coastal terrain to the south. This is consistent with YS's hypothesis of the lower coastal topography to the south resulting in attenuated low-level flow and convergence adjacent to the coast, which in turn weakened the precipitation. In addition, the tipped-forward baroclinic

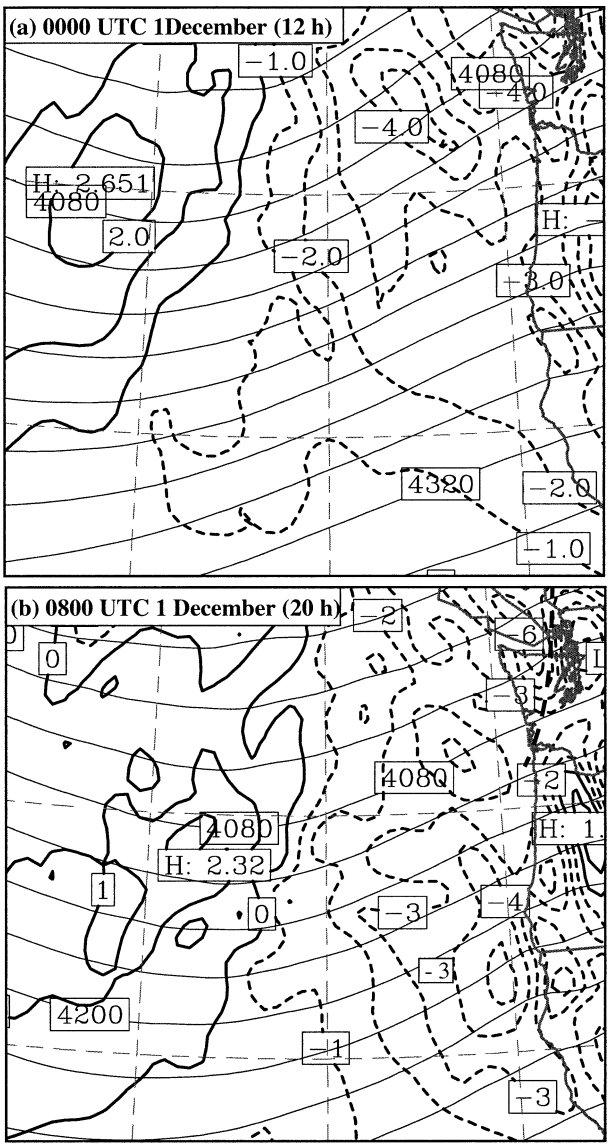

FIG. 15. Quasigeostrophic omega (ω) for the 700–500-mb layer for a portion of the 27-km domain at (a) 0000 and (b) 0800 UTC 1 Dec (contour interval of 1 dPa s^{-1}, with dashed lines indicating upward motion). The 600-mb geopotential heights are also contoured (solid) every 30 m.

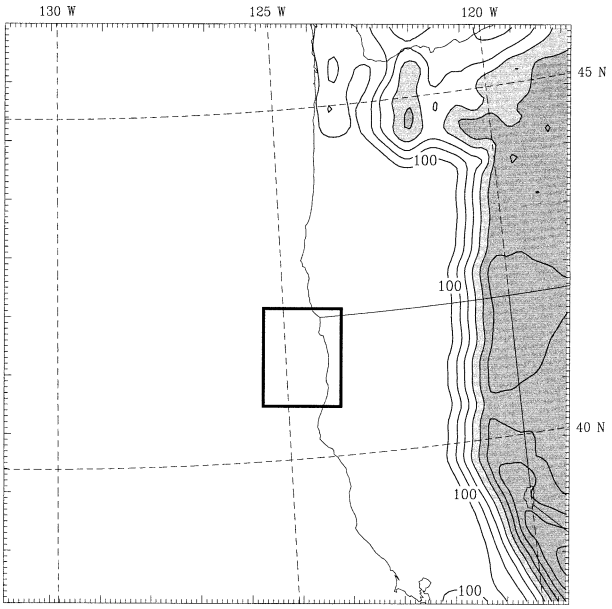

FIG. 16. Model terrain for the NCST experiment contoured every 300 m for 9-km domain. Terrain heights of 700–1000 m and greater than 1000 m are shaded light and dark gray, respectively. The boxed region shows the location of the frontogenesis calculations shown in Fig. 20.

structure between the surface and 850 mb in the NCST was not as apparent near CM (Fig. 18). Therefore, the enhanced southerly flow (produced by blocking) acted to retard the front's forward progression at low levels and thus contributed to the tipped-forward structure in the CTL. This tipped structure was also present well inland to the north at 0900 UTC, likely in response to blocking by the east slopes of the Sierra Nevada, located some 100–150 km farther east.

In order to emphasize differences in vertical structure between the CTL and NCST, Fig. 19 shows cross section AA′ as the front approached the coast, which can be compared with the CTL (Fig. 13). At 0500 UTC 1 December (Fig. 19a), there was a narrow band of weak ($<$30 dBZ) precipitation along the front that was weaker than the CTL at this time (Fig. 13a). The NCST along-barrier winds to the east of the front at low levels were 5–7 m s^{-1} weaker than those found in the CTL; therefore, the weaker frontal precipitation in the NCST run than the CTL strongly suggests that the coastal terrain acted to enhance the frontal precipitation well upstream (80 km) of the coast. There was a slight reduction in near-surface winds at the coast because of transition from water to land, which resulted in a weak upward motion and shallow precipitation enhancement focused along the coast. By 0700 and 0900 UTC 1 December (Figs. 19b,c), the NCST frontal precipitation had increased in areal coverage and intensity primarily because the large-scale forcing increased (cf. Fig. 15); however, the narrow intense bands of precipitation ($>$40 dBZ) failed to develop in the NCST run owing to the absence of enhanced upstream blocking and upslope flow. The temperature gradient and horizontal shear across the front were also weaker in the NCST as compared to the CTL.

c. Frontogenesis calculations

A number of theoretical studies have shown that fronts weaken as they move up windward slopes and conversely strengthen on the leeward side of barriers (Williams et al. 1992; Gross 1994; Li et al. 1996). More recent studies have shown that frontogenesis may also occur immediately upstream of the barrier associated with enhanced deformations during windward flow blocking (Braun et al. 1999a; Colle et al. 1999). Yu and Smull (2000) suggested that the barrier jet associated with flow blocking adjacent to the steep coastal terrain near the California–Oregon border enhanced the low-level convergence and rapid development of the NCFR in this region (cf., Fig. 5); however, YS did not have high-resolution temperature data required to calculate the potential frontogenesis associated with this process. The 3-km CTL simulation also showed a rapid development of the NCFR in this region (Fig. 10); therefore, an additional objective of our COAST IOP8 numerical study was to determine whether this enhancement was associated with an upstream terrain-induced frontogenetical process.

Using the 3-km model data, the various terms that can change the magnitude of the horizontal gradient of the potential temperature following an air parcel were evaluated on pressure levels using the Miller frontogenesis equation (Miller 1948):

$$\frac{d}{dt}|\nabla_h\theta| = \frac{-1}{|\nabla_h\theta|}\left\{\underbrace{\left[\left(\frac{\partial\theta}{\partial x}\right)^2\left(\frac{\partial u}{\partial x}\right) + \left(\frac{\partial\theta}{\partial y}\right)^2\left(\frac{\partial v}{\partial y}\right)\right]}_{\text{A}} + \underbrace{\left[\frac{\partial\theta}{\partial x}\frac{\partial\theta}{\partial y}\left(\frac{\partial v}{\partial x} + \frac{\partial u}{\partial y}\right)\right]}_{\text{B}} + \underbrace{\left[\frac{\partial\theta}{\partial z}\left(\frac{\partial w}{\partial x}\frac{\partial\theta}{\partial x} + \frac{\partial w}{\partial y}\frac{\partial\theta}{\partial y}\right)\right]}_{\text{B}}\right.$$

$$\left. - \underbrace{\left[\frac{\partial\theta}{\partial x}\frac{\partial}{\partial x}\left(\frac{d\theta}{dt}\right) + \frac{\partial\theta}{\partial y}\frac{\partial}{\partial y}\left(\frac{d\theta}{dt}\right)\right]}_{\text{C}}\right\}. \quad (1)$$

In (1), the three expressions on the right side are the deformation (A), tilting (B), and diabatic (C) terms, respectively. The diabatic term includes only heating/cooling from precipitation output from the 3-km domain. To assess low-level frontogenesis, the individual terms were calculated at 500 m ASL at 0800 UTC 1 December for the CTL and the NCST simulations (Fig. 20). The 500-m level was chosen since near the surface the fluxes from the relatively warm sea surface tended to mask the postfrontal temperature gradient.

At 0800 UTC 1 December (Fig. 20), the total frontogenesis along the front in the CTL simulation is largest within 100 km of the coast and at least four times greater than in the NCST run. Unlike the NCST simulation, the deformation term made a strong contribution to frontogenesis along the frontal zone in CTL, especially near the coast because of enhanced confluence forced by the terrain-enhanced flow. The differential diabatic effects from precipitation also contributed to significant frontogenesis along the front. In contrast, the differential vertical motion at the front results in a negative contribution (frontolysis) by the tilting term immediately west of the front. The diabatic term is greater than the tilting within 50 km of the coast, and dominates the total frontogenesis in this region. There is also net positive frontogenesis in the CTL simulation along the coast to the east of the front linked to the tilting term. This is associated with differential lifting associated with strong upslope flow just inland of the coast (cf. Fig. 13). In contrast, the frontogenesis terms are much weaker in NCST, with the negative and positive contributions from tilting and diabatic terms canceling each other.

In order to assess the reasons for the rapid frontal evolution in the coastal zone between 0300 and 1100 UTC 1 December, Fig. 21 shows the frontogenesis terms and the average potential temperature gradient at 500 m MSL within a 21 km $\times$ 90 km box following the front (cf. Fig. 20a). In this figure the frontogenesis evolution is also related to the average 500-m divergence within the box and the average model terrain height east of the box from the coast to the edge of the 3-km domain. Between 0300 and 0600 UTC, when the front was offshore and the large-scale forcing was relatively weak (cf. Fig. 15), the frontogenesis and low-level convergence contributions were small in both the CTL and NCST runs. As the front neared the coast between 0500 and 0900 UTC, the CTL frontogenesis adjacent to the steep terrain increased rapidly from 0.5 to 4.5 K (100 km h)$^{-1}$ while the NCST frontogenesis only increased to 1.5 K (100 km h)$^{-1}$. During this period the deformation strengthened as a result of increasing convergence between the terrain-enhanced flow and the front, as suggested by the differences between the CTL and NCST simulations (cf. Fig. 20). The enhanced convergence and associated precipitation along the front also resulted in diabatic frontogenesis dominating over the negative contributions from the tilting term. Between 0900 and 1100 UTC as the CTL front sagged south adjacent to lower topography and the coastal flow attenuated (cf., Fig. 15), the convergence and associated precipitation weakened. As a result, the total frontogenesis was less positive since the negative contributions from the tilting term dominated over diabatics and deformation frontogenesis no longer increased because of weaker convergent flow. Overall, these results support YS's hypothesis that decreased terrain blocking with the lower terrain to the south resulted in an attenuation of the NCFR.

d. No diabatic heating/cooling (NOLH, NOEVAP) experiments

The results above suggest that both terrain and diabatic effects may exert important influences on the frontal strength in the coastal zone. In order to further quantify the diabatic contributions to the observed evolution, separate simulations were conducted starting at forecast hour 12 of the CTL. An experiment designated NOLH allowed precipitation to occur but the latent heating/cooling effects were turned off (i.e., a so-called fake dry run), while a NOEVAP experiment turned off only the evaporative cooling from cloud and rainwater. In the NOLH experiment at 0700 UTC 1 December (Fig. 22a), a broad area of stratiform precipitation developed immediately offshore. As shown in other studies (Durran and Klemp 1983; Colle and Mass 1996), latent heating acts to reduce static stability near crest level. As a result of the increased static stabilities in the NOLH experiment, there was enhanced pressure ridging and upstream orographic precipitation along the coast as compared to the CTL (cf. Fig. 17a). The increased blocking slowed the forward progression of the front, but the frontal temperature gradients and wind shift were significantly *weaker* than those in the CTL. As suggested by the frontogenesis diagnostics, this indicates that terrain blocking was not the only important ingredient for the intensification of the landfalling front in the coastal zone. Rather, as shown in many previous studies (e.g., Knight and Hobbs 1988; Xu 1992), frontogenetical forcing combined with the release of conditional instability to produce banded convective precipitation with stronger ageostrophic motions, which in turn acted to intensify the front.

The NOEVAP experiment illustrates how much of the frontal organization was related to evaporative cooling effects, which have been shown to be important in strengthening the temperature gradient and precipitation development (Parker and Thorpe 1995b; Barth and Parsons 1996; Colle et al. 1999). With latent heating but no evaporative cooling present (Fig. 22b), convective precipitation develops and the structures are more similar to CTL than those found in the NOLH experiment. However, without evaporative cooling the frontal pre-

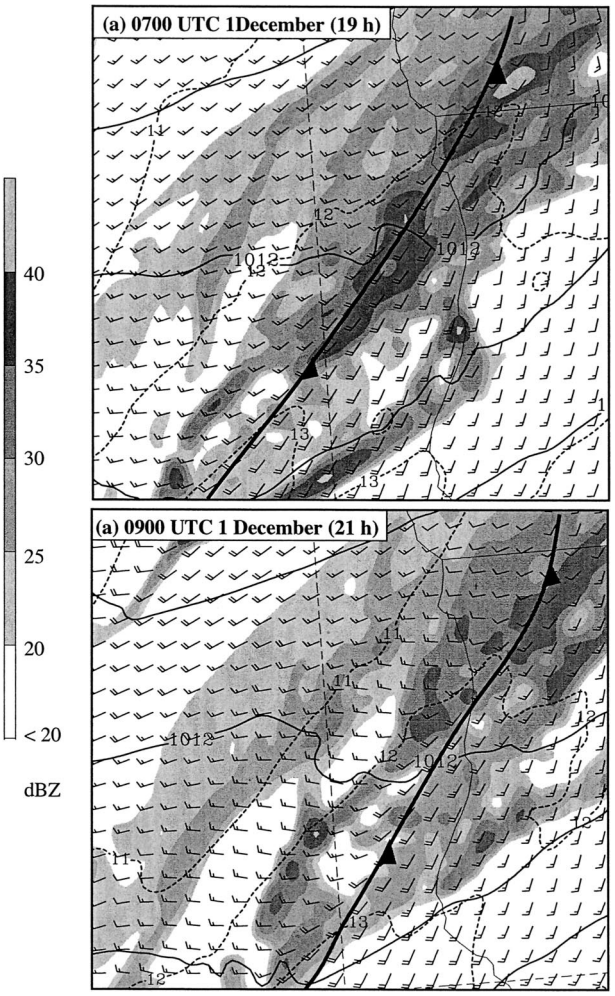

FIG. 17. Model surface analysis for the NCST 3-km simulation at (a) 0700 (19 h) and (b) 0900 UTC 1 Dec (21 h) showing sea level pressure (solid) every 1 mb, winds at 30 m above surface (1 full barb = 10 kt), 500-m temperatures (dashed) every 1°C, and model reflectivities (shaded).

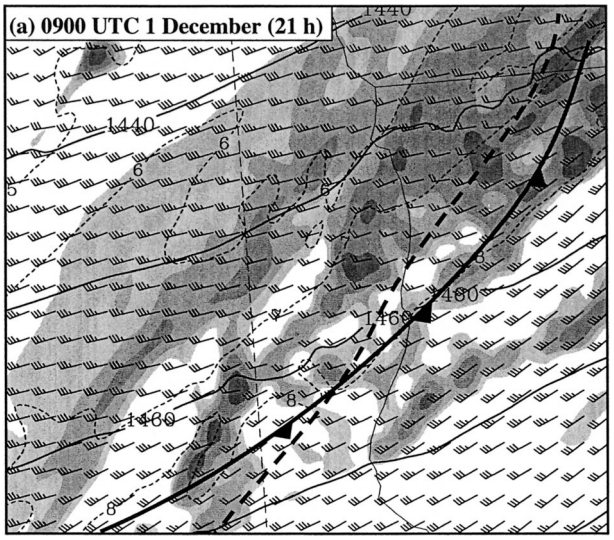

FIG. 18. Model 850-mb analysis for the NCST 3-km run at 0900 UTC 1 Dec (21 h), 850-mb geopotential heights (solid) every 10 m, winds (1 full barb = 10 kt), temperatures (dashed) every 1°C, and model reflectivities (shaded). The surface front is indicated by the bold dashed line.

cipitation band, temperature gradient, and wind shift are still less pronounced than the CTL, resulting in a slower and weaker front in the NOEVAP run. Overall, these results suggest that diabatic precipitation effects acted in combination with terrain influences to strengthen the front significantly more than the dry large-scale dynamics combined with terrain blocking effects.

6. Summary and conclusions

This paper constitutes an important extension of the previous work by Yu and Smull (2000, denoted YS), in which conventional synoptic observations as well as special profiler, ground-based, and NOAA P-3 Doppler airborne radar data were exploited to describe the mesoscale structure and evolution of a landfalling frontal system approaching the mountainous coastline of northern California on 1 December 1995. During this event, the frontal wind shift and precipitation were found to intensify rapidly as the low-level baroclinic zone approached a zone of steep coastal terrain. The goal of the study described here has been to use high-resolution mesoscale model simulations to describe the three-dimensional structures in the coastal zone and determine the responsible mechanisms for the rapid intensification of the front.

This event was simulated down to 3-km horizontal grid spacing using the Penn State–NCAR MM5. Many of its salient aspects were realistically reproduced, including the timing, location, and orientation of cold frontal features and associated precipitation development, as well as the tendency for the heaviest precipitation to occur near the coast, owing to an apparent superposition of frontal and orographic precipitation processes. Two notable weaknesses of the simulation were that the model's underestimate of the prefrontal terrain-enhanced flow magnitude by as much as 30%, and the tendency for the simulated front to be somewhat weaker than was observed.

The MM5 control simulation and subsequent experiments serve to illustrate the complex interrelationships among thermal, wind, and precipitation structures in the coastal zone. Prefrontal southwesterly flow was blocked by the steep coastal terrain, which led to development of a coastal mesoscale pressure ridge and a prefrontal southerly flow exceeding 25 m s^{-1}. Based on available airborne Doppler radar observations, YS suggested that the most profound influence of the coastal orography was within 20 km of the coast, which is significantly less than the 145-km Rossby radius predicted by theory ($N_m = 0.01$ s^{-1}, $h_m = 1400$ m, and $f = 9.75 \times 10^{-5}$

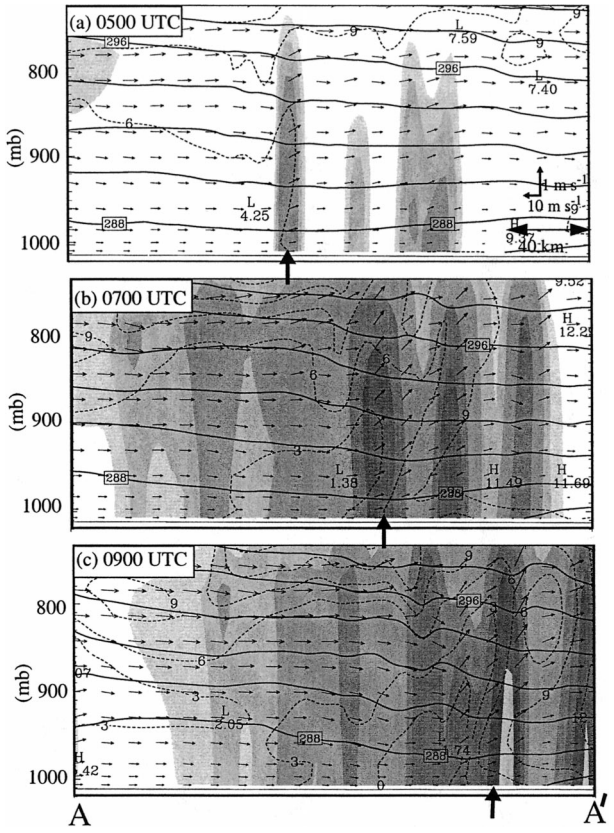

FIG. 19. Cross section AA′ for the NCST 3-km simulation at (a) 0500, (b) 0700, and (c) 0900 UTC 1 Dec 1995 showing potential temperature (solid every 2 K), model reflectivities (shaded using key in Fig. 11), north–south wind component (dashed every 3 m s^{-1}), and circulation winds (vectors) in the cross section. The surface frontal position is indicated by the bold arrow. The location of the cross sections are shown in Fig. 7b.

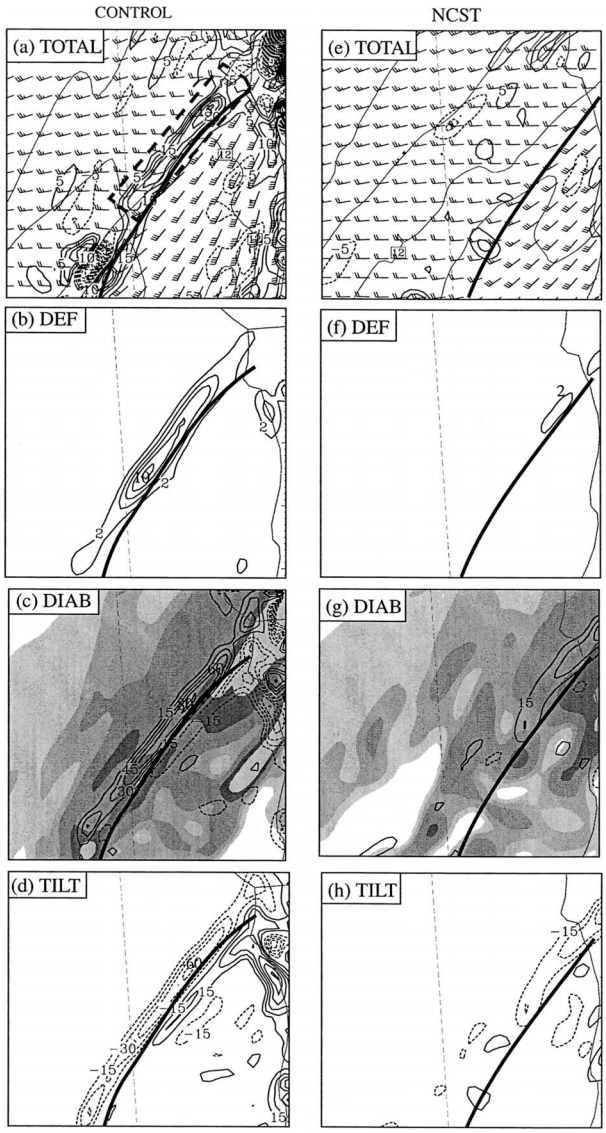

FIG. 20. (a) Total, (b) deformation, (c) diabatic, and (d) tilting frontogenesis (thick solid, positive; dashed, negative) for the CTL simulation for 500 MSL at 0800 UTC 1 Dec (20 h). The total is contoured every 5 K (100 km h)$^{-1}$, deformation every 2 K (100 km h)$^{-1}$, and diabatic and tilting every 15 K (100 km h)$^{-1}$. Winds (1 full barb = 10 kt) and 500-m temperatures (thin solid every 0.5°C) are shown for reference in (a), and model reflectivities (shaded using scale in Fig. 10) at 500 m are shown in (c). The model frontal position is shown by the bold solid line. (e)–(h) Same as in (a)–(d) except for the NCST simulation. The approximate geographic region shown for these calculations is given in Fig. 16. The dashed gray box in (a) is for the frontogenesis traces following the front shown in Fig. 21.

s^{-1}). However, the present, more comprehensive approach—including a model simulation without the coastal topography (designated the NCST run)—illustrates that significant orographic flow perturbations extended 80 km upwind of the coast, that is, more than 150 km from the crest of the inland terrain, and were thus in reasonable agreement with idealized theory. Because of the irregular coastline and highly three-dimensional terrain, the low-level coastal flow was not uniform in the north–south direction. Rather, prefrontal southerly flow decelerated downwind (north) of Cape Mendocino, while downgradient flow accelerations were both observed and simulated adjacent to segments of most steeply rising coastal topography. This illustrates that the local orographic effects, such as accelerations around bends in coastal topography or in association with mountain wakes, may play an important role in the structure and evolution of the flow in the coastal zone. Additional high-resolution field studies are needed to obtain high-resolution observations of the along-coast variability of the terrain enhanced flow.

The landfalling baroclinic surface trough evidently did not possess strong frontal characteristics a few hundred kilometers offshore. As this trough approached to within 100 km of the coast, it developed more baroclinic character—including a sharp low-level wind shift from southerly to westerly flow, a 1°–2°C (100 km)$^{-1}$ temperature drop, and an intense narrow cold frontal rainband (NCFR). The front was generally oriented from northeast to southwest; however, terrain blocking re-

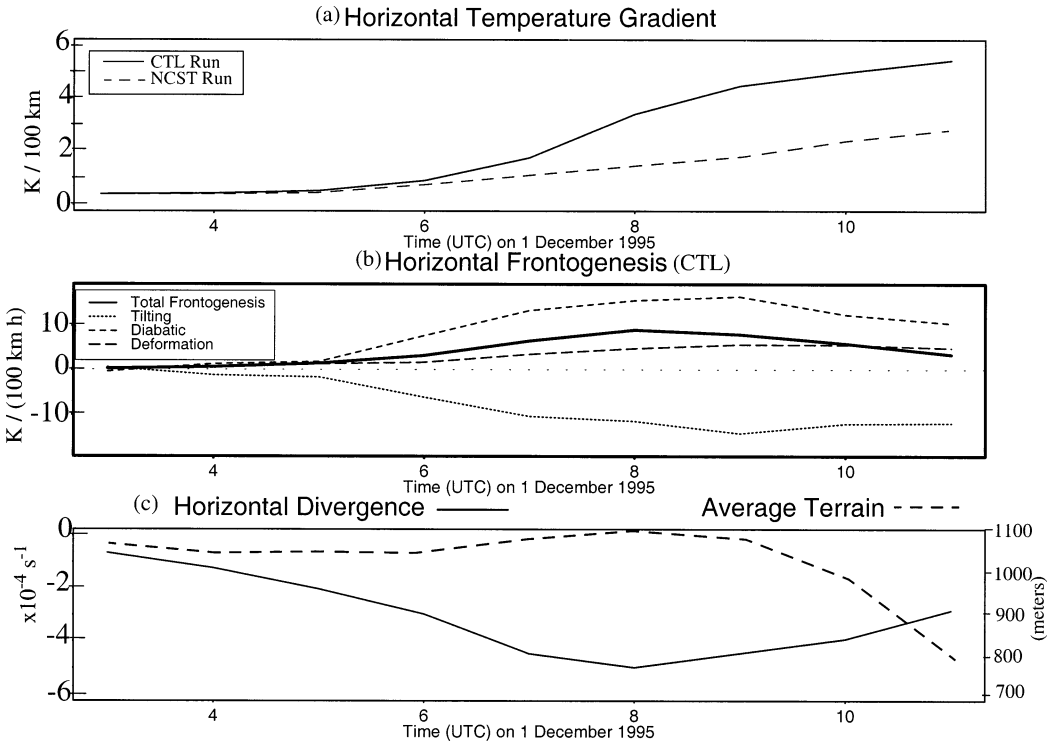

FIG. 21. Time series traces at 0.5 km MSL of the (a) CTL and NCST potential temperature gradient [K (100 km)$^{-1}$], (b) CTL frontogenesis terms {[K (100 km h)$^{-1}$], see inset for terms}, and (c) CTL horizontal divergence (10^{-4} s^{-1}) and average adjacent coastal terrain (m) for the box shown in Fig. 20a from 0300 to 2300 UTC 1 Dec 1995.

sulted in a locally perturbed alignment of the surface front as it neared the coast. Vertical sections illustrate that the front developed a 30–40-km tipped-forward frontal structure between the surface and 800 mb as it moved southward along the coast. In agreement with available observations, both the NCFR and frontal wind shift weakened in the simulation as the front moved southward adjacent to a region of lower coastal topography.

The MM5 allowed identification of specific mechanisms that led to rapid intensification of the frontal temperature gradient and precipitation in the coastal zone. Yu and Smull (2000) hypothesized that rapid intensification of low-level convergence and precipitation along the NCFR were the result of terrain blocking. The quasigeostrophic vertical velocity calculated from the MM5 for the 700–500-mb layer, however, was found to increase over the eastern Pacific as the upper-level trough approached the coast. This suggests that the large-scale forcing was generally favorable for the rapid development of precipitation in the coastal zone, albeit on much greater spatial/temporal scales than the observed/simulated banded precipitation features. This was further confirmed by a run in which the coastal terrain was artificially removed (NCST run), which showed a rapid development of widespread light to moderate coastal precipitation even in the absence of terrain effects. This trend toward increased large-scale forcing during the event appears to be linked to the ridging over the broad intermountain region of the western United States, which helped to shorten the wavelength of the upper-level trough, and in turn increase the upper-level forcing as the trough approached the coast. Later in the CTL run the large-scale upward motion was still significant; however, the frontal precipitation and low-level convergence rapidly weakened after 0900 UTC. Model results reproduce this weakening in a manner generally consistent with observations presented by YS, and confirm this notable evolutionary stage of the event was the result of subsequent reductions in orographic blocking as the front progressed southward beyond the region of steepest terrain.

Frontogenesis calculations show that the topographic features as far as 200 km distant from the coast (to the east) served to further enhance and collapse the NCFR and temperature gradients through increased deformation frontogenesis associated with the prefrontal terrain-enhanced flow. Diabatic effects from precipitation were also shown to be an important source of frontogenesis as the NCFR developed. This was further confirmed by a simulation without diabatic precipitation effects, which showed that both latent heating and cooling effects were also important in enhancing and organizing the precipitation and temperature gradients in the coastal zone. The tilting term was frontolytical at the front, but frontogenetical ahead of the front along the coast as a

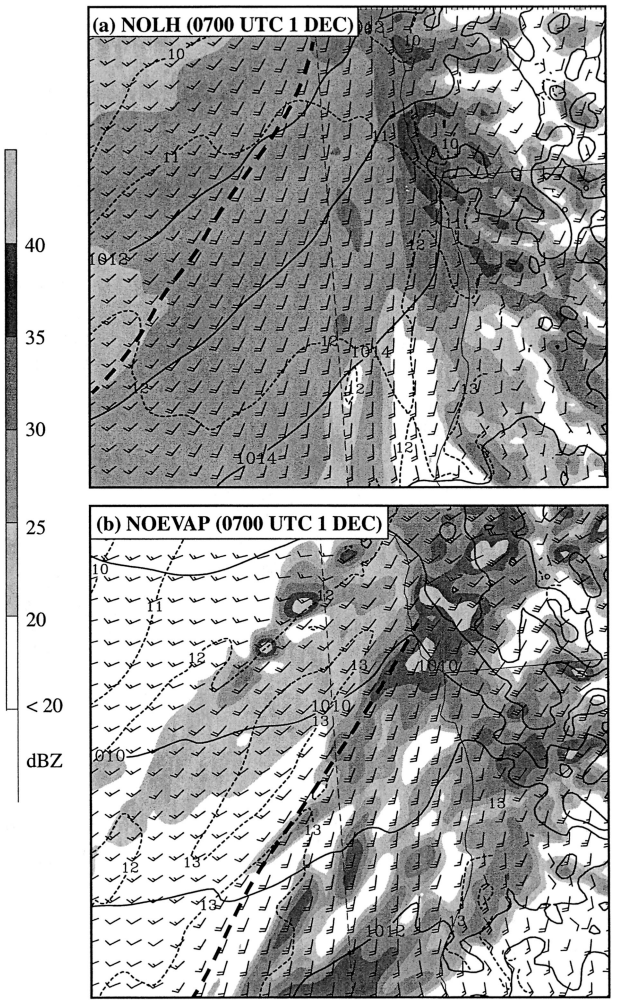

FIG. 22. Model 3-km surface analysis for the (a) NOLH and (b) NOEVAP experiments at 0700 UTC 1 Dec (19 h) showing sea level pressure (solid) every 1 mb, winds at 30 m above surface (1 full barb = 10 kt), 500-m temperatures (dashed) every 1°C, and model reflectivities (shaded).

result of an increase in upslope flow (vertical motion) to the east.

In summary, this study illustrates the complex, multiscale contributions to the rapid intensification and subsequent weakening of a landfalling front approaching the U.S. west coast as observed over a period of only a few hours. Well offshore, the precipitation and thermal gradients associated with the surface trough were relatively weak with little or no precipitation in evidence. As the large-scale vertical motions increased in an environment favoring moist convection, bands of fairly intense precipitation developed along the front in the coastal zone, with the NCFR and thermal gradients enhanced by the deformation associated with the terrain-enhanced flow along the coast. Meanwhile, diabatic effects associated with these bands helped to further intensify the low-level temperature gradients. Given the importance of heavy precipitation and peak winds to coastal and marine interests during these rapidly evolving landfalling frontal systems, it is clear that future work should emphasize additional high-resolution observations and representation of moist processes to better understand the feedback between the moist and dry dynamics for landfalling cyclonic storms.

Acknowledgments. This research was supported by the Office of Naval Research (Grants N00014-00-1-0407 and N00014-97-1-0707). Use of the MM5 was made possible by the Microscale and Mesoscale Meteorological Division of the National Center for Atmospheric Research, which is supported by the National Science Foundation. Comments and suggestions by Dr. Paul Neiman, Dr. Fred Sanders, and an anonymous reviewer significantly improved the manuscript.

REFERENCES

Barnes, S. L., F. Caracena, and A. Marroquin, 1996: Extracting synoptic-scale diagnostic information from mesoscale models: The Eta Model, gravity waves, and quasigeostrophic diagnostic. *Bull. Amer. Meteor. Soc.,* **77,** 519–528.

Barth, M. C., and D. B. Parsons, 1996: Microphysical processes associated with intense frontal rainbands and the effect of evaporation and melting on frontal dynamics. *J. Atmos. Sci.,* **53,** 1569–1586.

Benjamin, S. G., and N. L. Seaman, 1985: A simple scheme for objective analysis in curved flow. *Mon. Wea. Rev.,* **113,** 1184–1198.

Bond, N. A., and Coauthors, 1997: The Coastal Observation and Simulation with Topography (COAST) experiment. *Bull. Amer. Meteor. Soc.,* **78,** 1941–1955.

Braun, S. A., R. Rotunno, and J. B. Klemp, 1999a: Effects of coastal orography on landfalling cold fronts. Part I: Dry, invisid dynamics. *J. Atmos. Sci.,* **56,** 517–533.

——, ——, and ——, 1999b: Effects of coastal orography on landfalling cold fronts. Part II: Effects of surface friction. *J. Atmos. Sci.,* **56,** 3366–3384.

Buzzi, A., N. Tartaglione, and P. Malguzzi, 1998: Numerical simulations of the 1994 Piedmont flood: Role of orography and moist processes. *Mon. Wea. Rev.,* **126,** 2369–2383.

Colle, B. A., and C. F. Mass, 1996: An observational and modeling study of the interaction of low-level southwesterly flow with the Olympic Mountains during COAST IOP4. *Mon. Wea. Rev.,* **124,** 2152–2175.

——, ——, and B. F. Smull, 1999: An observational and numerical study of a cold front interacting with the Olympic Mountains during COAST IOP5. *Mon. Wea. Rev.,* **127,** 1310–1334.

Doyle, J. D., 1997: The influence of mesoscale orography on a coastal jet and rainband. *Mon. Wea. Rev.,* **125,** 1465–1488.

Durran, D. R., and J. B. Klemp, 1982: On the effects of moisture on the Brunt–Väisälä frequency. *J. Atmos. Sci.,* **39,** 2152–2158.

——, and ——, 1983: A compressible model for the simulation of moist mountain waves. *Mon. Wea. Rev.,* **111,** 2341–2351.

Fovell, R. G., and Y. Ogura, 1988: Numerical simulation of a midlatitude squall line in two dimensions. *J. Atmos. Sci.,* **45,** 3846–3879.

Gross, B. D., 1994: Frontal interaction with isolated orography. *J. Atmos. Sci.,* **51,** 1480–1496.

Hoskins, B. J., I. Draghici, and H. C. Davies, 1978: A new look at the ω-equation. *Quart. J. Roy. Meteor. Soc.,* **104,** 31–38.

Kain, J. S., and J. M. Fritsch, 1990: A one-dimensional entraining/detraining plume model and its application in convective parameterization. *J. Atmos. Sci.,* **47,** 2784–2802.

Klemp, J. B., and D. R. Durran, 1983: An upper boundary condition

permitting internal gravity wave radiation in numerical mesoscale models. *Mon. Wea. Rev.*, **111,** 430–444.

Knight, D. J., and P. V. Hobbs, 1988: The mesoscale and microscale structure and organization of clouds and precipitation in midlatitude cyclones: A numerical modeling study of frontogenesis and cold frontal rainbands. *J. Atmos. Sci.*, **45,** 915–930.

Li, S.-W., M. S. Peng, and R. T. Williams, 1996: A three-dimensional study of the influence of mountains on a front. *J. Atmos. Sci.*, **53,** 2757–2772.

Miller, J. E., 1948: On the concept of frontogenesis. *J. Meteor.*, **5,** 169–171.

Okland, H., 1990: The dynamics of coastal troughs and coastal fronts. *Tellus*, **42A,** 444–462.

Overland, J. E., and N. A. Bond, 1995: Observations and scale analysis of coastal wind jets. *Mon. Wea. Rev.*, **123,** 2934–2941.

Parker, D. J., and A. J. Thorpe, 1995a: Conditional convective heating in a baroclinic atmosphere: A model of convective frontogenesis. *J. Atmos. Sci.*, **52,** 1699–1711.

——, and ——, 1995b: The role of snow sublimation in frontogenesis. *Quart. J. Roy. Meteor. Soc.*, **121,** 763–782.

Pierrehumert, R. T., and B. Wyman, 1985: Upstream effects of mesoscale mountains. *J. Atmos. Sci.*, **42,** 977–1003.

Reisner, J., R. M. Rasmussen, and R. T. Bruintjes, 1998: Explicit forecasting of supercooled liquid water in winter storms using the MM5 mesoscale model. *Quart. J. Roy. Meteor. Soc.*, **124,** 1071–1107.

Roeloffzen, J. C., W. D. van Den Berg, and J. Oerlemans, 1986: Frictional convergence at coastlines. *Tellus*, **38A,** 397–411.

Rotunno, R., J. B. Klemp, and M. L. Weisman, 1988: A theory for strong, long-lived squall lines. *J. Atmos. Sci.*, **45,** 463–485.

Schumacher, P. N., D. J. Knight, and L. F. Bosart, 1996: Frontal interaction with the Appalachian Mountains. Part I: A climatology. *Mon. Wea. Rev.*, **124,** 2453–2468.

Stauffer, D. R., and N. L. Seaman, 1990: Use of four-dimensional data assimilation in a limited-area mesoscale model. Part I: Experiments with synoptic-scale data. *Mon. Wea. Rev.*, **118,** 1250–1277.

——, ——, and F. S. Binkowski, 1991: Use of four-dimensional data assimilation in a limited-area mesoscale model. Part II: Effects of data assimilation within the planetary boundary layer. *Mon. Wea. Rev.*, **119,** 734–754.

Stoelinga, M. T., J. D. Locatelli, and P. V. Hobbs, 2000: Structure and evolution of winter cyclones in the central United States and their effects on the distribution of precipitation. Part VI: A mesoscale modeling study of the initiation of convective rainbands. *Mon. Wea. Rev.*, **128,** 3481–3500.

Williams, R. T., M. S. Peng, and D. A. Zankofski, 1992: Effects of topography on fronts. *J. Atmos. Sci.*, **49,** 287–305.

Xu, Q., 1992: Formation and evolution of frontal rainbands and geostrophic potential vorticity anomalies. *J. Atmos. Sci.*, **49,** 629–648.

Yu, C.-K., and B. F. Smull, 2000: Airborne observations of a landfalling cold front upstream of steep coastal orography. *Mon. Wea. Rev.*, **128,** 1577–1603.

Zhang, D., and R. A. Anthes, 1982: A high-resolution model of the planetary boundary layer—Sensitivity test and comparisons with SESAME-79 data. *J. Appl. Meteor.*, **21,** 1594–1609.